Mathematical model and numerical analysis method for dynamic fracture in a residual stress field

Sayako Hirobe [1,*] Kenji Imakita,[2] Haruo Aizawa,[2] Yasumasa Kato,[3] Shingo Urata [3] and Kenji Oguni [1,†]

[1]*Research Institute for Value-Added Information Generation, Japan Agency for Marine-Earth Science and Technology, Yokohama, Kanagawa 236-0001, Japan*
[2]*Materials Integration Laboratories, AGC Inc., Yokohama, Kanagawa 221-0863, Japan*
[3]*Innovative Technology Laboratories, AGC Inc., Yokohama, Kanagawa 230-0045, Japan*

Residual stress field is a self-equilibrium state of stress in the bulk solid material with the inhomogeneous field of the inelastic deformations. The high level of tensile residual stress often leads to dynamic fracture resulting in the instantaneous and catastrophic destruction of the materials because the cracks are fed with the strain energy initially stored in the bulk materials due to the residual stress. The dissipation of the strain energy with crack growth results in the release and the redistribution of the residual stress. In this paper, we propose an effective mathematical model and a numerical analysis method for dynamic fracture in residual stress field. We formulate the dynamic behavior of solid continuum with residual stress field in the context of particle discretization scheme finite element method. This formulation enables the appropriate evaluation of (i) release and redistribution of residual stress due to dynamic propagation of the cracks and (ii) the effect of the elastic wave on crack propagation, which are the most substantial problems on dynamic fracture in residual stress field. We perform the experiments and the simulations of dynamic fracture process in chemically tempered glass sheets with residual stress field to validate the proposed numerical analysis method. The simulation results show remarkable agreement with the experiments of the catastrophic failure of the glass sheets with residual stress field in all aspects of crack behavior. These results indicate that the proposed model and method can rigorously evaluate the release and the autonomous redistribution of the residual stress in the dynamic fracture process.

I. INTRODUCTION

Residual stress field is a self-equilibrated state of stress induced by the inhomogeneous distribution of the inelastic deformations, temperature and moisture gradients or local volume changes due to phase transition. Since the compressive residual stress has the ability to prevent crack initiation and growth, the intentional introduction of the surface compressive residual stress by surface machining or finishing process (e.g., quenching, cold working, and shot-peening) has been utilized for a significant increase in the apparent tensile strength of the bulk materials. While compressive residual stress significantly improves the material resistance, tensile residual stress produces high stress concentration at crack tips and promotes failure. Hence, the unintentional accumulation of the tensile residual stress usually results in undesired geometrical distortion and unexpected reduction of the strength of the bulk materials.

In contrast to the fracture phenomena usually treated in the basic fracture mechanics theory, cracks in tensile residual stress fields have the possibility for the dynamic growth without any persistent external loading. This is because cracks are fed with the strain energy initially stored in the bulk materials due to the residual stress. Therefore, the high level of tensile residual stress promotes the significant acceleration of the crack propagation resulting in the instantaneous and catastrophic destruction of the bulk materials.

The most typical examples of the catastrophic failure due to residual stress field are observed in tempered glass. Since glass is an amorphous solid exhibiting perfect linear elasticity and brittle fracture at normal temperature, the tempered glass is a suitable material for investigating the dynamic fracture in residual stress field. The tempered glass improves the resistance to the surface flaws and to the external loads by introducing the compressive residual stress [1,2] at the surface of the glass through the chemical [3–5] or thermal treatment [6,7]. However, because of the self-equilibrium constraint on the stress field, any compressive residual stress must be accompanied by the tensile residual stress and thereby the smooth residual stress profile is introduced within the thickness of the tempered glass sheet; see Fig. 1. Thus, if a flaw manages to reach the tensile stress region through the compressive surface layer, it becomes a trigger of the catastrophic failure and shatters the tempered glass sheet into small diced fragments [8–11].

The dynamic crack propagation in tempered glass sheets has attracted much attention over this half century from the perspectives of product safety and scientific interest. The majorities of these early works are experiment-based investigations using the high-speed photography or the high-speed color photoelastic picture to capture the dynamic fracture process in residual stress field [12–15]. However, the release

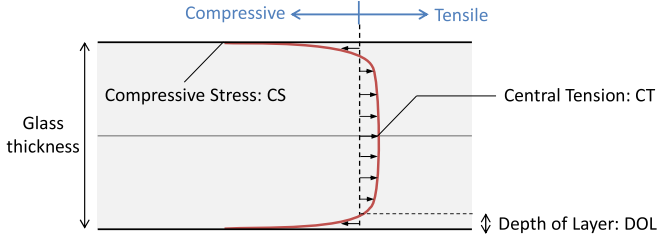*hirobes@jamstec.go.jp
†ogunik@jamstec.go.jp

FIG. 1. The residual stress profile within the thickness of the chemically tempered glass sheet.

and the redistribution of the residual stress field due to the dynamic fracture is still hardly observable because the systems and devices for the full-field measurement of the stress field (e.g., digital image correlation (DIC) [16–18], high-speed digital photoelasticity [13,15,19–21]) are limited on the evaluation of the outer-surface residual stress field (DIC) or the residual stress intensity averaged over the thickness of the specimen (photoelasticity). Moreover, the crack propagation, the change in residual stress field, and the elastic wave are complicatedly entangled with each other in dynamic fracture process. This complicated entanglement also brings substantial theoretical complexity. This is why numerical approaches are required for the assessment of the dynamic fracture in residual stress field.

Although many experimental investigations and analytical studies for building phenomenological models can be found, there exist only a few numerical and computational studies for the fracture process in tempered glass (e.g., a quasistatic fracture model for describing a single crack evolution in tempered glass sheets [22] and a quasistatic finite-element model for estimating the remaining strain energy in fragments [23,24]). In spite of these efforts for numerical evaluation of the fracture in residual stress field, the achievement of the previous works is only confined to the evaluation of the quasistatic propagation of a single crack. In these two decades, many fracture analysis methods such as eXtended finite-element method [25–27], FEM with cohesive zone model [28,29], phase field method [30,31], and peridynamics [32,33] have been proposed. These enhanced numerical analysis methods have been successfully applied to a wide variety of fracture phenomena. Nevertheless, the numerical analysis of multiple crack propagation in residual stress field is still highly challenging. This is mainly because of the difficulty in capturing the change in the residual stress field due to dynamic fracture.

The purpose of this paper is to propose an effective mathematical model and a numerical analysis method for dynamic fracture in the residual stress field. We formulate the dynamic behavior of solid continuum with residual stress field in the context of particle discretization scheme finite element method (PDS-FEM) developed by the authors [34–37]. This formulation enables the appropriate evaluation of (i) release and redistribution of the residual stress due to dynamic propagation of the cracks and (ii) the effect of the elastic wave on crack propagation, which are the most substantial problems in dynamic fracture in the residual stress field. For evaluating the validity of the proposed mathematical model and numerical analysis method, we performed experiments and numerical

analyses of the self-driven dynamic fracture process in chemically tempered glass sheets with different residual stress profiles in the thickness direction. The overview of this study is given in Hirobe *et al.* [38].

II. FORMULATION OF PARTICLE DISCRETIZATION SCHEME FINITE ELEMENT METHOD

A. Problem setting

Consider a problem for the infinitesimal deformation of the homogeneous isotropic linearly elastic body Ω. When the displacement boundary condition $\bar{u}_i(\boldsymbol{x})$ is imposed on the boundary of Ω (denoted as $\partial\Omega$), the boundary value problem for the displacement $u_i(\boldsymbol{x})$ is

$$\begin{cases} \sigma_{ij,j}(\boldsymbol{x}) + b_i(\boldsymbol{x}) = 0 & \boldsymbol{x} \in \Omega \\ \sigma_{ij}(\boldsymbol{x}) = c_{ijkl}\epsilon_{kl}(\boldsymbol{x}) & \boldsymbol{x} \in \Omega \\ \epsilon_{ij}(\boldsymbol{x}) = \frac{1}{2}(u_{i,j}(\boldsymbol{x}) + u_{j,i}(\boldsymbol{x})) & \boldsymbol{x} \in \Omega \\ u_i(\boldsymbol{x}) = \bar{u}_i(\boldsymbol{x}) & \boldsymbol{x} \text{ on } \partial\Omega \end{cases}, \quad (1)$$

where σ_{ij} is a stress tensor, ϵ_{kl} is a strain tensor, c_{ijkl} is an elasticity tensor, u_i is a displacement vector, and b_i is a body force vector. The summation convention is employed for subscripts throughout this paper.

This boundary value problem for the displacement u_i is equivalent to the variational problem in which the following functional J of the displacement field $u_i(\boldsymbol{x})$ should be made stationary:

$$\mathrm{J}[u_i(\boldsymbol{x})] = \int_\Omega \left(\frac{1}{2}\epsilon_{ij}c_{ijkl}\epsilon_{kl} - b_i u_i \right) dV. \quad (2)$$

Here the first term of the integrant in Eq. (2) is the strain energy density. Introducing the displacement-strain relationship $\epsilon_{ij} = \frac{1}{2}(u_{i,j} + u_{j,i})$ to the functional in Eq. (2), only the displacement vector u_i is explicitly included in the functional J. Thus, the displacement vector u_i which satisfies the stationary condition $\delta\mathrm{J} = 0$ and the prescribed displacement boundary condition $u_i(\boldsymbol{x}) = \bar{u}_i(\boldsymbol{x})$ for $\boldsymbol{x}$ on $\partial\Omega$ is the solution of the boundary value problem (1).

B. Particle discretization scheme

For the numerical evaluation of the functional J in Eq. (2), PDS-FEM applies the particle discretization scheme to the field variables. The analysis domain $\Omega \in \mathbb{R}^3$ is discretized in different ways by a pair of conjugate geometries corresponding to a set of nodes $\{\boldsymbol{x}^\alpha \mid \alpha \in \mathbb{N}, 1 \leqslant \alpha \leqslant N\}$ as follows:

$$\hat{\Omega} = \sum_{\alpha=1}^{N} \Phi^\alpha, \quad (3)$$

$$\hat{\Omega} = \sum_{\beta=1}^{M} \Psi^\beta, \quad (4)$$

where $\{\Phi^\alpha \mid \alpha \in \mathbb{N}, 1 \leqslant \alpha \leqslant N\}$ is a set of the Voronoi tessellations, whereas $\{\Psi^\beta \mid \beta \in \mathbb{N}, 1 \leqslant \beta \leqslant M\}$ is a set of the Delaunay tessellations, and $\hat{\Omega}$ is the discretized analysis domain. The Delaunay tessellation becomes a set of triangles in the two-dimensional case and becomes a set of tetrahedrons in
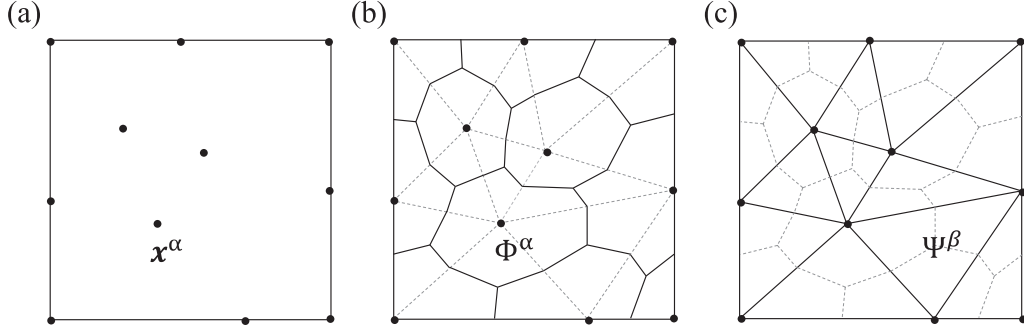
FIG. 2. The Voronoi and the Delaunay tessellations in the two-dimensional case, (a) seed points, (b) Voronoi tessellations, and (c) Delaunay tessellations.

the three-dimensional case; see, for instance, Fig. 2 in the two-dimensional setting. The definition of Voronoi tessellations employed in PDS-FEM is slightly different from the original definition of the Voronoi tessellation. The Voronoi edges are connecting the gravity centers of the Delaunay edges, areas (and volumes for three-dimensional case).

The field variables are discretized on the spatially discretized analysis domain $\hat{\Omega}$ by using the following characteristic functions on the Voronoi tessellations and the Delaunay tessellations.

$$\phi^{\alpha}(\boldsymbol{x}) = \begin{cases} 1 & (\boldsymbol{x} \in \Phi^{\alpha}) \\ 0 & (\boldsymbol{x} \notin \Phi^{\alpha}) \end{cases}, \tag{5}$$

$$\psi^{\beta}(\boldsymbol{x}) = \begin{cases} 1 & (\boldsymbol{x} \in \Psi^{\beta}) \\ 0 & (\boldsymbol{x} \notin \Psi^{\beta}) \end{cases}. \tag{6}$$

These discontinuous and nonoverlapping characteristic functions enable the easy treatment of the discontinuous field due to fracture. The displacement field is discretized on the Voronoi tessellations as

$$u_i(\boldsymbol{x}) = \sum_{\alpha=1}^{N} u_i^{\alpha} \phi^{\alpha}(\boldsymbol{x}), \tag{7}$$

where u_i^{α} is the nodal displacement vector of the αth node. The body force $b_i(\boldsymbol{x})$ is likewise discretized on the Voronoi tessellations as

$$b_i(\boldsymbol{x}) = \sum_{\alpha=1}^{N} b_i^{\alpha} \phi^{\alpha}(\boldsymbol{x}), \tag{8}$$

where b_i^{α} is the nodal body force vector of the αth node. The physical quantities related to the spatial derivatives of the displacement field are discretized on the Delaunay tessellations as

$$\epsilon_{ij}(\boldsymbol{x}) = \sum_{\beta=1}^{M} \epsilon_{ij}^{\beta} \psi^{\beta}(\boldsymbol{x}), \tag{9}$$

$$\sigma_{ij}(\boldsymbol{x}) = \sum_{\beta=1}^{M} \sigma_{ij}^{\beta} \psi^{\beta}(\boldsymbol{x}), \tag{10}$$

where ϵ_{ij}^{β} and σ_{ij}^{β}, respectively, denotes the element strain tensor and the element stress tensor for the βth element. When the elasticity tensor c_{ijkl} is a function of the position $\boldsymbol{x}$, $c_{ijkl}(\boldsymbol{x})$

is discretized as

$$c_{ijkl}(\boldsymbol{x}) = \sum_{\beta=1}^{M} c_{ijkl}^{\beta} \psi^{\beta}(\boldsymbol{x}). \tag{11}$$

According to these discretizations, the displacement field is expressed as the translational motion of the rigid body particles defined by the Voronoi tessellations. Thus, PDS gives a particle description to the displacement field while strain and stress fields are averaged and evaluated over the Delaunay tessellations (which is a conjugate set of the Voronoi tessellations).

Consider a tetrahedron Ψ^{β} (composed of Φ^{α}, Φ^{γ}, Φ^{ζ}, and Φ^{ξ}) shown in Fig. 3. In the framework of PDS, the displacement-strain matrix $B_i^{\beta\alpha}$ for this tetrahedral element
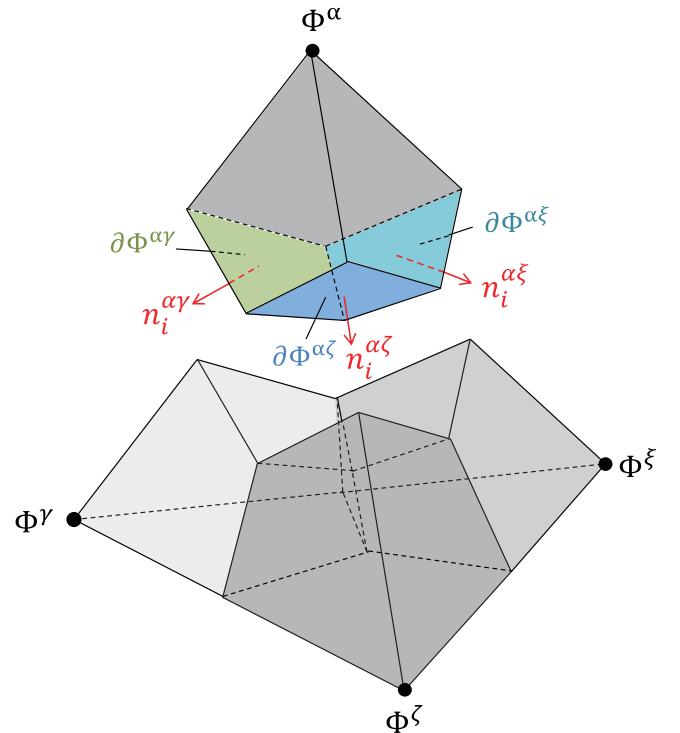

FIG. 3. A Delaunay tetrahedron Ψ^{β} composed of Φ^{α}, Φ^{γ}, Φ^{ζ}, and Φ^{ξ}.

Ψ^β is given as

$$
\begin{aligned}
B_i^{\beta\alpha} &= \frac{1}{\Psi^\beta} \int_{\Psi^\beta} \phi_{,i}^\alpha \psi^\beta dV \\
&= \frac{1}{\Psi^\beta} \int_{\partial\Psi^\beta} n_i^\alpha dS \\
&= \frac{1}{\Psi^\beta} \int_{\partial\Phi^\alpha \cap \Psi^\beta} n_i^\alpha dS \\
&= \frac{1}{\Psi^\beta} \left(\int_{\partial\Phi^{\alpha\gamma} \cap \Psi^\beta} n_i^{\alpha\gamma} dS + \int_{\partial\Phi^{\alpha\zeta} \cap \Psi^\beta} n_i^{\alpha\zeta} dS \right. \\
&\quad \left. + \int_{\partial\Phi^{\alpha\xi} \cap \Psi^\beta} n_i^{\alpha\xi} dS \right),
\end{aligned} \tag{12}
$$

where $\partial\Phi^{\alpha\gamma}$ is the boundary of the αth Voronoi tessellation adjacent to the γth Voronoi tessellation, and $n_i^{\alpha\gamma}$ is the outward unit normal vector of the αth Voronoi tessellation on $\partial\Phi^{\alpha\gamma}$ (likewise for $\partial\Phi^{\alpha\zeta}$, $\partial\Phi^{\alpha\xi}$, $n_i^{\alpha\zeta}$, and $n_i^{\alpha\xi}$). By using this displacement-strain matrix $B_i^{\beta\alpha}$, the discretized displacement-strain relationship is expressed as

$$
\epsilon_{ij}^\beta = \sum_{\alpha=1}^N \frac{1}{2}\left(B_j^{\beta\alpha} u_i^\alpha + B_i^{\beta\alpha} u_j^\alpha \right). \tag{13}
$$

In spite of the discontinuous characteristic functions used for the discretization of the displacement field $u_i(\boldsymbol{x})$, the components of $B_i^{\beta\alpha}$ are identical to those of the displacement-strain matrix for the conventional FEM of tetrahedral elements with linear interpolation functions.

C. PDS-FEM

Applying the particle discretization scheme for the functional J in Eq. (2), PDS-FEM can be formulated. The discretized functional $\hat{\mathrm{J}}$ is

$$
\begin{aligned}
\hat{\mathrm{J}}\left(u_i^\alpha, \epsilon_{ij}^\beta\right) &= \sum_{\beta=1}^M \frac{1}{2} \epsilon_{ij}^\beta c_{ijkl} \epsilon_{kl}^\beta \Psi^\beta - \sum_{\alpha=1}^N b_i^\alpha u_i^\alpha \Phi^\alpha \\
&= \sum_{\alpha=1}^N \sum_{\gamma=1}^N \frac{1}{2} K_{ik}^{\alpha\gamma} u_i^\alpha u_k^\gamma - \sum_{\alpha=1}^N b_i^\alpha u_i^\alpha \Phi^\alpha, \quad (14)
\end{aligned}
$$

where Ψ^β is used for the volume of the βth Delauanay tessellation, Φ^α is used for the volume of the αth Voronoi tessellation, and $K_{ik}^{\alpha\gamma}$ is the stiffness matrix defined as

$$
K_{ik}^{\alpha\gamma} = \sum_{\beta=1}^M B_j^{\beta\alpha} c_{ijkl}^\beta B_l^{\beta\gamma} \Psi^\beta. \tag{15}
$$

Because of the identity of the displacement-strain matrix $B_i^{\beta\alpha}$ used in PDS-FEM and the conventional FEM, the stiffness matrix expressed as Eq. (15) is also identical to that of the conventional FEM of tetrahedral elements with linear interpolation functions.

Since the stiffness matrix $K_{ik}^{\alpha\gamma}$ is a positive definite matrix, the variational problem for the functional in Eq. (2) results in the minimization problem for the quadratic function in Eq. (14). Therefore, the approximate solution for the boundary value problem (1) is a set of the nodal displacement $\{u_i^\alpha\}$ corresponding to the stationary point of the quadric surface.

This approximate solution is given by solving the following simultaneous equations for $\{u_i^\alpha\}$ obtained from the stationary condition $\partial\hat{\mathrm{J}}/\partial u_i^\alpha$ for the discretized functional $\hat{\mathrm{J}}$:

$$
\sum_{\gamma=1}^N K_{ik}^{\alpha\gamma} u_k^\gamma - b_i^\alpha \Phi^\alpha = 0. \tag{16}
$$

Thus, PDS-FEM leads to the same simultaneous equations as the conventional FEM of tetrahedral elements with linear interpolation functions. In spite of the usage of the discontinuous displacement field (i.e., translational motion of the rigid body particles) in PDS-FEM, the approximate solution for the boundary value problem (1) obtained by PDS-FEM is identical to that obtained by the conventional FEM of tetrahedral elements with linear interpolation functions [34]. In this sense, PDS-FEM provides the rigorous description for the particle model with the perfect correspondence to the deformable solid continuum.

This particle description of the displacement field in a deformable solid continuum provides us a simple and rigorous simulation of the fracture surfaces. In PDS-FEM, the fracture is expressed as the loss of the interaction between two adjacent Voronoi particles. This loss of the interaction corresponds to the removal of the surface integral in Eq. (12) on the fractured Voronoi boundary. For instance, when the boundary between the αth Voronoi particle Φ^α and the γth Voronoi particle Φ^γ is fractured, the surface integral of the unit normal vector becomes zero on $\partial\Phi^{\alpha\gamma}$ in the Delaunay tetrahedron Ψ^β related to $\partial\Phi^{\alpha\gamma}$:

$$
\int_{\partial\Phi^{\alpha\gamma} \cap \Psi^\beta} n_i^{\alpha\gamma} dS = 0 \ \ \forall \alpha, \beta, \gamma \ \text{s.t.} \ \partial\Phi^{\alpha\gamma} \ \text{in} \ \Psi^\beta \ \text{is fractured.}
$$

$$
\tag{17}
$$

III. HAMILTONIAN FORMULATION OF PDS-FEM FOR THE DYNAMIC BEHAVIOR OF THE DEFORMABLE SOLID CONTINUUM

In this section, we extend PDS-FEM to the problem for the dynamic behavior of the solid continuum through the Hamiltonian formulation. PDS-FEM expresses the solid continuum as a set of rigid body particles defined by the Voronoi tessellations $\{\Phi^\alpha\}$. This particle expression enables the definition of the Hamiltonian for the deformable solid continuum as follows.

Let m^α be the mass of the αth Voronoi particle and let $\dot{u}_i^\alpha$ be the velocity for the translational motion of the mother point of the αth Voronoi particle, $\boldsymbol{x}^\alpha$. Then the total kinetic energy of the whole discretized body $\hat{\Omega}$, denoted as T, is given as the sum of the kinetic energy of each Voronoi particle:

$$
T(\dot{u}_i^\alpha) = \sum_{\alpha=1}^N \frac{1}{2} m^\alpha \dot{u}_i^\alpha \dot{u}_i^\alpha. \tag{18}
$$

In three-dimensional case, since the αth Voronoi particle is composed of the set of a quarter region of a Delaunay tessellation (see the quarter region of a Delaunay tessellation in Fig. 3), the volume of the αth Voronoi particle V_{Φ^α} is

expressed as

$$V_{\Phi^\alpha} = \sum_{\substack{\beta \\ \Phi^\alpha \cap \Psi^\beta \neq \emptyset}} V_{\Psi^\beta}/4. \tag{19}$$

Then m^α is given as $m^\alpha = \rho V_{\Phi^\alpha}$, where ρ is the mass density.

The potential energy is stored by the deformation of the solid continuum due to the displacement of the Voronoi particles. Then, the total potential energy stored in $\hat{\Omega}$, denoted as V, is given as the sum of the strain energy accumulated in each Delaunay tetrahedron due to the relative displacement between the Voronoi particles:

$$V(u_i^\alpha) = \sum_{\alpha=1}^N \sum_{\gamma=1}^N \frac{1}{2} K_{ij}^{\alpha\gamma} u_i^\alpha u_j^\gamma, \tag{20}$$

where $K_{ij}^{\alpha\gamma}$ is the stiffness matrix defined in Eq. (15). Note that a body force b_i is ignored hereafter for the sake of simplicity.

In general, the Lagrangian L for a system of particles is defined as $L = T - V$, where T is the total kinetic energy of the system and V is the total potential energy of the system. Here, given a Lagrangian L in terms of the generalized coordinates $\boldsymbol{q}^\alpha$ and the generalized velocities $\dot{\boldsymbol{q}}^\alpha$, the Hamiltonian H is derived from the Legendre transformation of the Lagrangian L. Then $H = \sum_\alpha \boldsymbol{p}^\alpha \cdot \dot{\boldsymbol{q}}^\alpha - L$, where $\boldsymbol{p}^\alpha$ is the generalized momentum.

When the coordinate system for the set of the Voronoi particles are fixed, the generalized coordinates q_i^α and the generalized velocities $\dot{q}_i^\alpha$ correspond to the displacement of the Voronoi particles and the velocity of the Voronoi particles, respectively:

$$q_i^\alpha = u_i^\alpha, \tag{21}$$

$$\dot{q}_i^\alpha = \dot{u}_i^\alpha. \tag{22}$$

Then, the Lagrangian L for the set of the Voronoi particles is

$$\begin{aligned} L &= T(\dot{q}_i^\alpha) - V(q_i^\alpha) \\ &= \sum_{\alpha=1}^N \frac{1}{2} m^\alpha \dot{q}_i^\alpha \dot{q}_i^\alpha + \sum_{\alpha=1}^N \sum_{\gamma=1}^N \frac{1}{2} K_{ij}^{\alpha\gamma} q_i^\alpha q_j^\gamma \end{aligned} \tag{23}$$

and the generalized momentum p_i^α is

$$p_i^\alpha = \frac{\partial L}{\partial \dot{q}_i^\alpha} = m^\alpha \dot{q}_i^\alpha. \tag{24}$$

Therefore, the Hamiltonian H for the motion of the set of the Voronoi particles is given as

$$\begin{aligned} H &= T(p_i^\alpha) + V(q_i^\alpha) \\ &= \sum_{\alpha=1}^N \frac{1}{2m^\alpha} p_i^\alpha p_i^\alpha + \sum_{\alpha=1}^N \sum_{\gamma=1}^N \frac{1}{2} K_{ij}^{\alpha\gamma} q_i^\alpha q_j^\gamma. \end{aligned} \tag{25}$$

Regarding this Hamiltonian H, the time evolution of this system of the Voronoi particles is uniquely defined by Hamiltonian equations as

$$\dot{q}_i^\alpha = \frac{\partial H}{\partial p_i^\alpha} = \frac{p_i^\alpha}{m^\alpha} = \dot{u}_i^\alpha, \tag{26}$$

$$\dot{p}_i^\alpha = -\frac{\partial H}{\partial q_i^\alpha} = -\sum_{\gamma=1}^N K_{ij}^{\alpha\gamma} q_j^\gamma = -\sum_{\gamma=1}^N K_{ij}^{\alpha\gamma} u_j^\gamma. \tag{27}$$

IV. INTRODUCTION OF RESIDUAL STRESS FIELD INTO PDS-FEM FORMULATION

The residual stress is released and redistributed during the dynamic fracture process. Therefore, the appropriate evaluation of the change in the residual stress field is essential for the prediction of the crack path in bulk materials with residual stress field. Introduction of the residual stress field into the Hamiltonian formulation of PDS-FEM enables us the appropriate treatment of the release of the residual stress and the autonomous redistribution of the residual stress.

A. Particle discretization of residual stress field

The residual stress field is the resultant of the elastic strain field for keeping a self-equilibrium state of stress in the bulk material with the permanent and inhomogeneous inelastic deformations [39,40]. For a bulk solid material with the permanent and inhomogeneous inelastic deformations, let the permanent inelastic strain be ϵ_{ij}^p and the elastic strain be ϵ_{ij}^e. Then, the total strain ϵ_{ij}^t which represents the total deformation from the initial (deformation-free) state is defined as

$$\epsilon_{ij}^t = \epsilon_{ij}^e + \epsilon_{ij}^p. \tag{28}$$

Since the elastic strain ϵ_{ij}^e is the only source of the residual stress in the bulk solid material, the residual stress σ_{ij} is given as

$$\sigma_{ij} = c_{ijkl}\epsilon_{kl}^e = c_{ijkl}\big(\epsilon_{kl}^t - \epsilon_{kl}^p\big). \tag{29}$$

Here all the strains which does not contribute to the generation of the elastic stress (i.e., residual stress) in the linear elastic material are referred to as the permanent inelastic strain ϵ_{kl}^p.

Consider a problem for the homogeneous isotropic linearly elastic body Ω with the prescribed distribution of the permanent inelastic strain ϵ_{ij}^p in Ω. The deformation of Ω is governed by the following boundary value problem for the total displacement $u_i^t(\boldsymbol{x})$:

$$\begin{cases} \sigma_{ij,j}(\boldsymbol{x}) = 0 & \boldsymbol{x} \in \Omega \\ \sigma_{ij}(\boldsymbol{x}) = c_{ijkl}\big[\epsilon_{kl}^t(\boldsymbol{x}) - \epsilon_{kl}^p(\boldsymbol{x})\big] & \boldsymbol{x} \in \Omega \\ \epsilon_{ij}^t(\boldsymbol{x}) = \frac{1}{2}\big[u_{i,j}^t(\boldsymbol{x}) + u_{j,i}^t(\boldsymbol{x})\big] & \boldsymbol{x} \in \Omega \\ u_i^t(\boldsymbol{x}) = \bar{u}_i^t(\boldsymbol{x}) & \boldsymbol{x} \text{ on } \partial\Omega \end{cases}, \tag{30}$$

where u_i^t is the displacement vector corresponding to the total strain ϵ_{ij}^t. This boundary value problem for the total displacement u_i^t is equivalent to the following variational problem where the functional J of the total displacement field $u_i^t(\boldsymbol{x})$ has to be made stationary:

$$\begin{aligned} \mathrm{J} &= \int_\Omega \frac{1}{2} \epsilon_{ij}^e c_{ijkl} \epsilon_{kl}^e dV \\ &= \int_\Omega \frac{1}{2}\big(\epsilon_{ij}^t - \epsilon_{ij}^p\big) c_{ijkl}\big(\epsilon_{kl}^t - \epsilon_{kl}^p\big) dV. \end{aligned} \tag{31}$$

Thus, the total displacement vector u_i^t which satisfies the stationary condition $\delta\mathrm{J} = 0$ and the prescribed displacement boundary condition $u_i^t(\boldsymbol{x}) = \bar{u}_i^t(\boldsymbol{x})$ for $\boldsymbol{x}$ on $\partial\Omega$ is the solution of the boundary value problem (30).

Then, we apply the particle discretization proposed in PDS-FEM for the functional J. The discretized functional $\hat{J}$ is

$$
\hat{J} = \sum_{\beta=1}^{M} \frac{1}{2} \left(\epsilon_{ij}^{t\beta} - \epsilon_{ij}^{p\beta} \right) c_{ijkl} \left(\epsilon_{kl}^{t\beta} - \epsilon_{kl}^{p\beta} \right) \Psi^{\beta}
$$
$$
= \sum_{\beta=1}^{M} \left(\frac{1}{2} \epsilon_{ij}^{t\beta} c_{ijkl} \epsilon_{kl}^{t\beta} - \epsilon_{ij}^{p\beta} c_{ijkl} \epsilon_{kl}^{t\beta} + \frac{1}{2} \epsilon_{ij}^{p\beta} c_{ijkl} \epsilon_{kl}^{p\beta} \right) \Psi^{\beta}.
$$
(32)

The approximate solution of the boundary value problem (30) is a set of the nodal displacement $\{u_i^{t\alpha}\}$ which satisfies the stationary condition for $\hat{J}$. Introducing the discretized displacement-strain relationship [Eq. (13)] with respect to the total strain tensor in the βth element $\epsilon_{ij}^{t\beta}$, the discretized functional $\hat{J}$ is expressed in terms of $u_i^{t\alpha}$. Then, the stationary condition $\partial \hat{J} / \partial u_i^{t\alpha}$ for the discretized functional $\hat{J}$ gives the following simultaneous equations for $\{u_i^{t\alpha}\}$:

$$
\sum_{\gamma=1}^{N} K_{ik}^{\alpha\gamma} u_k^{t\gamma} = f_i^{\alpha},
$$
(33)

where

$$
f_i^{\alpha} = \sum_{\beta=1}^{M} B_j^{\beta\alpha} c_{ijkl}^{\beta} \epsilon_{kl}^{p\beta} \Psi^{\beta}.
$$
(34)

Since the right-hand side of Eq. (34) consists of the spatial derivative operator $B_j^{\beta\alpha}$ and the permanent inelastic strain $\epsilon_{kl}^{p\beta}$, f_i^{α} can be interpreted as a nodal force due to the spatial distribution of the permanent inelastic strain. Thus, Eq. (33) clearly states that the source of the residual stress is the spatial distribution of the permanent inelastic strain $\epsilon_{kl}^{p\beta}$. When Ω is in self-equilibrium state without external applied loadings, the resultant force of the whole domain is zero (i.e., $\sum_{\alpha=1}^{N} f_i^{\alpha} = 0$).

B. Dynamic behavior of the solid continuum with residual stress field

According to the particle discretization of the residual stress field, the Hamiltonian for the dynamic behavior of the solid continuum with the residual stress field can be defined in the same procedure proposed in Sec. III.

Here the generalized coordinates q_i^{α}, the generalized velocities $\dot{q}_i^{\alpha}$, and the generalized momentum p_i^{α} are

$$
q_i^{\alpha} = u_i^{t\alpha},
$$
(35)

$$
\dot{q}_i^{\alpha} = \dot{u}_i^{t\alpha},
$$
(36)

$$
p_i^{\alpha} = m^{\alpha} \dot{q}_i^{\alpha} = m^{\alpha} \dot{u}_i^{t\alpha}.
$$
(37)

The total potential energy stored in the system of the Voronoi particles with the residual stress field, denoted as $V(q_i^{\alpha})$, is identical to the strain energy shown in Eq. (32). Since the third term in the parentheses of the right-hand side of Eq. (32) is not related to $q_i^{\alpha} (= u_i^{t\alpha})$, the Hamiltonian H for the motion of the system of the Voronoi particles with the residual stress field is given as

$$
H = T(p_i^{\alpha}) + V(q_i^{\alpha})
$$
$$
= \sum_{\alpha=1}^{N} \frac{1}{2m^{\alpha}} p_i^{\alpha} p_i^{\alpha} + \sum_{\alpha=1}^{N} \sum_{\gamma=1}^{N} \frac{1}{2} K_{ij}^{\alpha\gamma} q_i^{\alpha} q_j^{\gamma} - \sum_{\alpha=1}^{N} f_i^{\alpha} q_i^{\alpha}.
$$
(38)

Based on this Hamiltonian, the time evolution of the system of the Voronoi particles with the residual stress field is given by the following Hamiltonian equations:

$$
\dot{q}_i^{\alpha} = \frac{\partial H}{\partial p_i^{\alpha}} = \frac{p_i^{\alpha}}{m^{\alpha}} = \dot{u}_i^{t\alpha},
$$
(39)

$$
\dot{p}_i^{\alpha} = -\frac{\partial H}{\partial q_i^{\alpha}} = -\sum_{\gamma=1}^{N} K_{ij}^{\alpha\gamma} q_j^{\gamma} + f_i^{\alpha} = -\sum_{\gamma=1}^{N} K_{ij}^{\alpha\gamma} u_j^{t\gamma} + f_i^{\alpha},
$$
(40)

where f_i^{α} is the nodal force given by Eq. (34). In these Hamiltonian equations, the effect of the permanent inelastic strain $\epsilon_{kl}^{p\beta}$ is introduced as the nodal force f_i^{α} to the time evolution of the momentum. When the system of the Voronoi particles is in the static equilibrium state, the right-hand side of Eq. (40) becomes zero from Eq. (33).

C. Fracture criterion and the change in the field due to fracture

From the view point of the energy balance, the Griffith energy criterion states that a crack propagates when the released potential energy by crack growth is greater than or equal to the surface energy for creating the new crack surfaces [41]. This criterion poses the following specified condition for the crack growth: new cracks are created when $G \geqslant 2\Gamma$ is satisfied, where G is the energy release rate for the crack growth and Γ is the surface energy.

In PDS-FEM, the minimum unit for the expression of the fracture surfaces is the boundary between two adjacent Voronoi particles. Therefore, focusing on the boundary between two adjacent Voronoi particles $\partial \Phi^{\alpha\gamma}$, the energy release rate G is given as $G = \Delta U / S$, where ΔU is the released potential energy of the total system due to fracture of $\partial \Phi^{\alpha\gamma}$ and S is the area of $\partial \Phi^{\alpha\gamma}$. Then we can set the following fracture criterion in the framework of PDS-FEM: When $\Delta U / S \geqslant 2\Gamma$ is satisfied, the boundary between the two adjacent Voronoi particles $\partial \Phi^{\alpha\gamma}$ is fractured.

Since PDS-FEM expresses the fracture as a change in the components of the displacement-strain matrix related to the fractured Voronoi boundary, the only source of ΔU is the change in the elastic strain energy of the Delaunay regions including the fracture surfaces. As shown in Fig. 4, when the Voronoi particle boundary $\partial \Phi^{\alpha\gamma}$ is included in the κth Delaunay region Ψ^{κ} and the λth Delaunay region Ψ^{λ}, the released potential energy of the total system due to the fracture of $\partial \Phi^{\alpha\gamma}$ is

$$
\Delta U = \sum_{\beta=\kappa,\lambda} \left(\frac{1}{2} \epsilon_{ij}^{e\beta} c_{ijkl} \epsilon_{kl}^{e\beta} \Psi^{\beta} - \frac{1}{2} \epsilon_{ij}^{e\beta*} c_{ijkl} \epsilon_{kl}^{e\beta*} \Psi^{\beta} \right),
$$
(41)

where the superscript $*$ represents the variables and the matrices in fractured Delaunay regions and Ψ^{β} is the volume (area
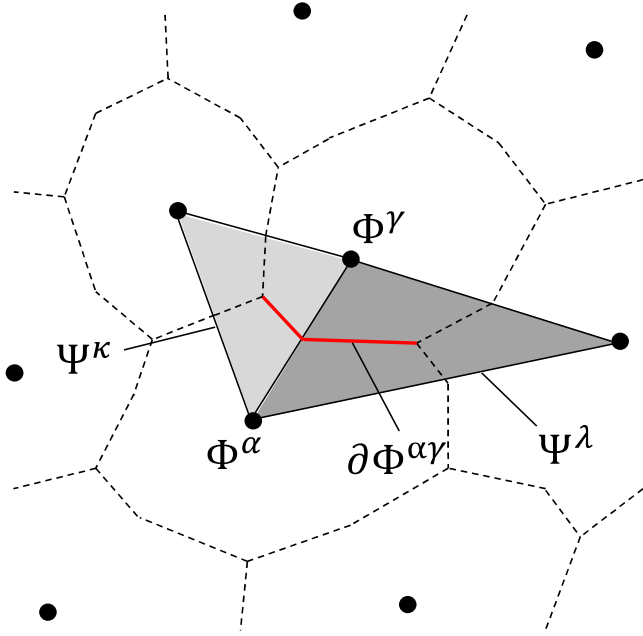
FIG. 4. Delaunay triangles Ψ^κ and Ψ^λ including a fractured Voronoi boundary $\partial\Phi^{\alpha\gamma}$.

TABLE I. CT, CS, and DOL for chemically tempered glass sheets used in the experiment.

	CT (MPa)	CS (MPa)	DOL (μm)
case I	52.0	836	39.0
case II	75.0	806	55.0
case III	112	752	80.0

V. DYNAMIC FRACTURE EXPERIMENT OF CHEMICALLY TEMPERED GLASS SHEETS

To obtain the reference experiment data set for evaluating the validity of the proposed mathematical model and numerical analysis method, we performed fracture experiment of the chemically tempered glass sheets.

A. Experimental procedure

The in-plane residual stress distribution of the chemically tempered glass sheet is volumetric and uniform (i.e., $\sigma_{xx} = \sigma_{yy} = $ const, $\sigma_{xy} = 0$ when the thickness direction is set to be the z direction) and the out-plane residual stress is zero (i.e., $\sigma_{zz} = 0$). The residual stress profile in the thickness direction is characterized by the compressive residual stress at the outer surface, referred to as compressive stress (CS), the tensile residual stress at the midplane in the thickness direction, referred to as central tension (CT), and the depth of the compression layer, referred to as Depth of layer (DOL); see Fig. 1. Since the crack propagation is driven by the tensile residual stress, the fracture process of the chemically tempered glass sheet strongly depends on CT and DOL.

In the experiment, we used three types of chemically tempered glass sheets with different residual stress profiles. The chemical tempering process performed in this study is as follows. We firstly prepared the thin rectangular float glass sheets with the size of $l_x \times l_y \times l_z = 50 \times 2.0 \times 0.70$ mm. Then, we chemically strengthened these float glass sheets by exchanging Na^+ for K^+. The ion exchange process was performed by immersing the glass in 100 % KNO_3 salt bath at 450 °C. Since invading K^+ is larger in size than Na^+, this ion exchange leads to the high surface compression and balancing interior tension depending on the diffusion length of K^+ and the glass thickness. Here, we used the chemically tempered glass sheets with the immersing time of 2 h, 4 h, and 9 h. The compressive layer becomes deeper (i.e., DOL has larger value) as the immersing time becomes longer. These three types of chemically tempered glass sheets are respectively named as case I, case II, and case III. The values of CT, CS, and DOL for each chemically tempered glass sheet are shown in Table I. The values of CT were derived from the approximate calculation using the measured values of DOL and CS.

Each of these three types of chemically tempered glass sheets was set on the bottom of the trajectory of the free fall pendulum so that the sheet face was vertical to the ground and the long side was parallel to the ground; see schematic view of the experimental system in Fig. 5. The fracture was initiated from the short side of the chemically tempered glass sheet by the collision of the impactor of the pendulum. The
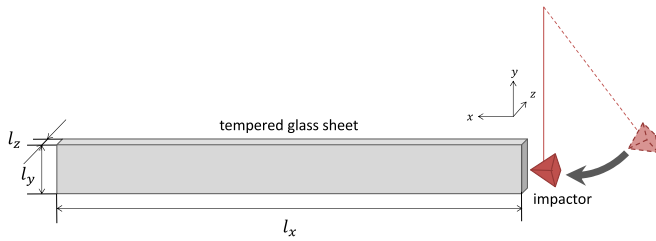
for the two-dimensional problem) of the βth Delaunay region. Figure 4 and Eq. (41) show the two-dimensional case for the sake of simplicity. The derivation of $\epsilon_{ij}^{e\beta*}$ should be referred to Appendix A.

When the boundary between the two adjacent Voronoi particles $\partial\Phi^{\alpha\gamma}$ is fractured, the displacement-strain matrix $B_j^{\beta\alpha}$ and the stiffness matrix $K_{ik}^{\alpha\gamma}$ related to $\partial\Phi^{\alpha\gamma}$ are modified by Eq. (17). In the dynamic problems, this modification of the matrices is embedded in the Hamiltonian equation (40) obtaining the time evolution of the momentum of each Voronoi particle. In particular, the nodal force f_i^α becomes

$$f_i^\alpha = \sum_{\beta=1}^M B_j^{\beta\alpha*} c_{ijkl}^\beta \epsilon_{kl}^{p\beta*} \Psi^\beta$$

$$\forall \alpha, \beta, \gamma \text{ s.t. } \partial\Phi^{\alpha\gamma} \text{ in } \Psi^\beta \text{ is fractured.} \quad (42)$$

The derivation of $\epsilon_{kl}^{p\beta*}$ is in Appendix A.

Thus, the only source of the change in the Hamiltonian by the fracture (i.e., the energy dissipation due to fracture) is the loss of the potential energy in the elements with newly created crack surfaces.

When the initial cracks are introduced into the self-equilibrated residual stress field, the static equilibrium state Eq. (33) is broken by the modification of the force vector f_i^α shown in Eq. (42) and by the modification of the components of the stiffness matrix $K_{ik}^{\alpha\gamma}$ due to Eq. (17). In this unbalanced state, the right-hand side of Eq. (40) is no longer equal to zero and the system of Voronoi particles starts to exhibit the dynamic behavior. This is how the release and the autonomous redistribution of the residual stress in the fracture process can be rigorously evaluated in the proposed model and numerical analysis method.

FIG. 5. The schematic view of the experimental system.

impactor was the square pyramidal indenter with $100°$ face angle and the approximate impact energy was 44 mJ. The energy of the impactor was same for all the experiments. The collision of the impactor has no significant influence on the dynamic fracture process of the chemically tempered glass sheets because this collision does not cause catastrophic failure of the annealed glass sheets. The fracture process was recorded from the perpendicular direction to the sheet face by the high-speed video camera (SHIMADZU HPV X2) with the recording speed of 5 000 000 fps. The width of the field of view of the high-speed video camera was about 8–10 mm from the impact surface.

B. Results of dynamic fracture experiment

Figure 6 shows the crack patterns of the chemically tempered glass sheets with different residual stress profile. Here we show two samples for each case. Supplemental Videos 1–3 [42] show the crack propagation process recorded by the high-speed camera for case I-1, II-1, and III-1, respectively. The black triangle appearing from the right edge is the impactor which collides with the chemically tempered glass sheet to start the fracture process. These figures and videos show the crack patterns projected on the *xy* plane. As seen in Fig. 6,

the crack patterns change depending on the residual stress profile. In case I, the only one crack smoothly proceeds until it reaches the edge of the glass sheet. As CT increases, the crack starts branching. In case II, the initially growing crack branches once to three and only the main crack extends long. The other two cracks grow from the center toward the edge of the glass sheet soon after branching. In both case I and II, the cracks do not fully propagate through the entire length of the specimen and they terminate when they reach to the edge of the glass sheet. In case III, the fracture patterns are completely different from those in case I and II. The cracks in case III repeatedly branch and continue to propagate until the glass sheet is completely fractured. This catastrophic failure of the glass sheet is only observed in case III, i.e., under the high tensile residual stress field. Based on these experiments, we can confirm that the residual stress profile has strong influence on the fracture pattern. In addition to these features of crack patterns depending on the residual stress profile, an interesting crack morphology is observed in these experiments. As seen in all cases (noticeable in case III), the cracks form the fanlike shape when they approach the edge of the glass sheet. However, merely from the experimental observation, it is difficult to infer how this fanlike shape is formed.

Figure 7 shows the crack velocity of the chemically tempered glass sheets in the experiments. The crack velocity was measured by using the JPEG images of the crack propagation process. We took the snapshots for the crack propagation at the constant time step $\Delta t_v = 200$ ns and recorded the pixel position at the tip of the main crack. The propagating distance in Δt_v was derived by the linear interpolation between the positions at t and $t + \Delta t_v$. For case I, the crack velocity transitions about between 1500 and 2000 m/s. However, for case II and III, the crack velocity almost reaches or exceeds 2000 m/s. At this point, the cracks branch and the crack
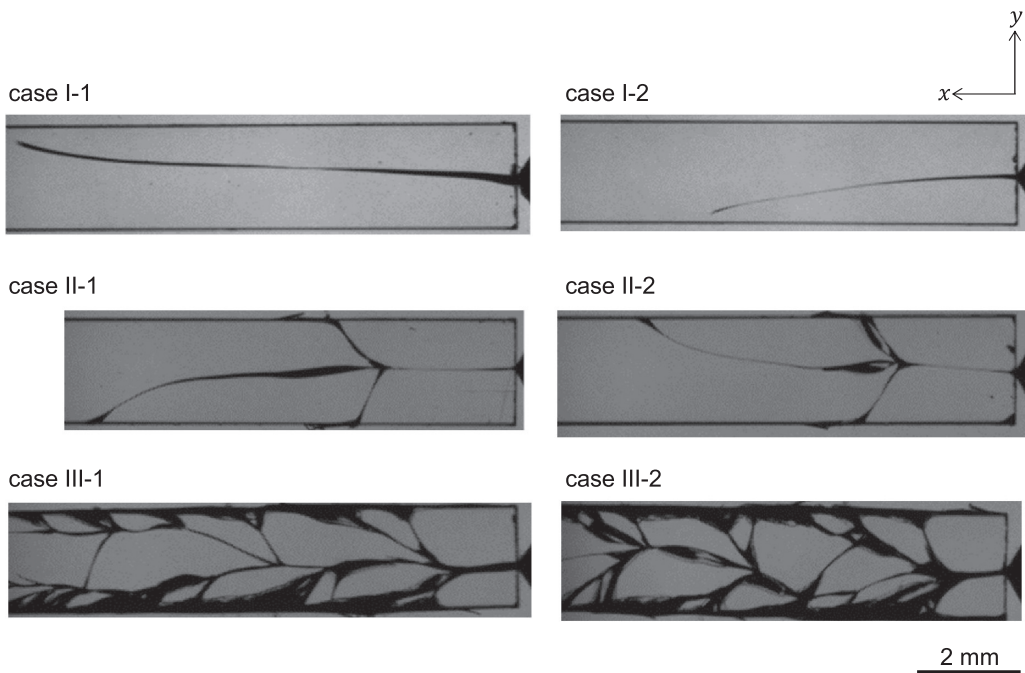

FIG. 6. Crack patterns of the chemically tempered glass sheets in the experiments. The width of the field of view of the experiments is about 8–10 mm from the impact surface. The snapshots are at the time when the cracks stop or reach at the end of the field of view.
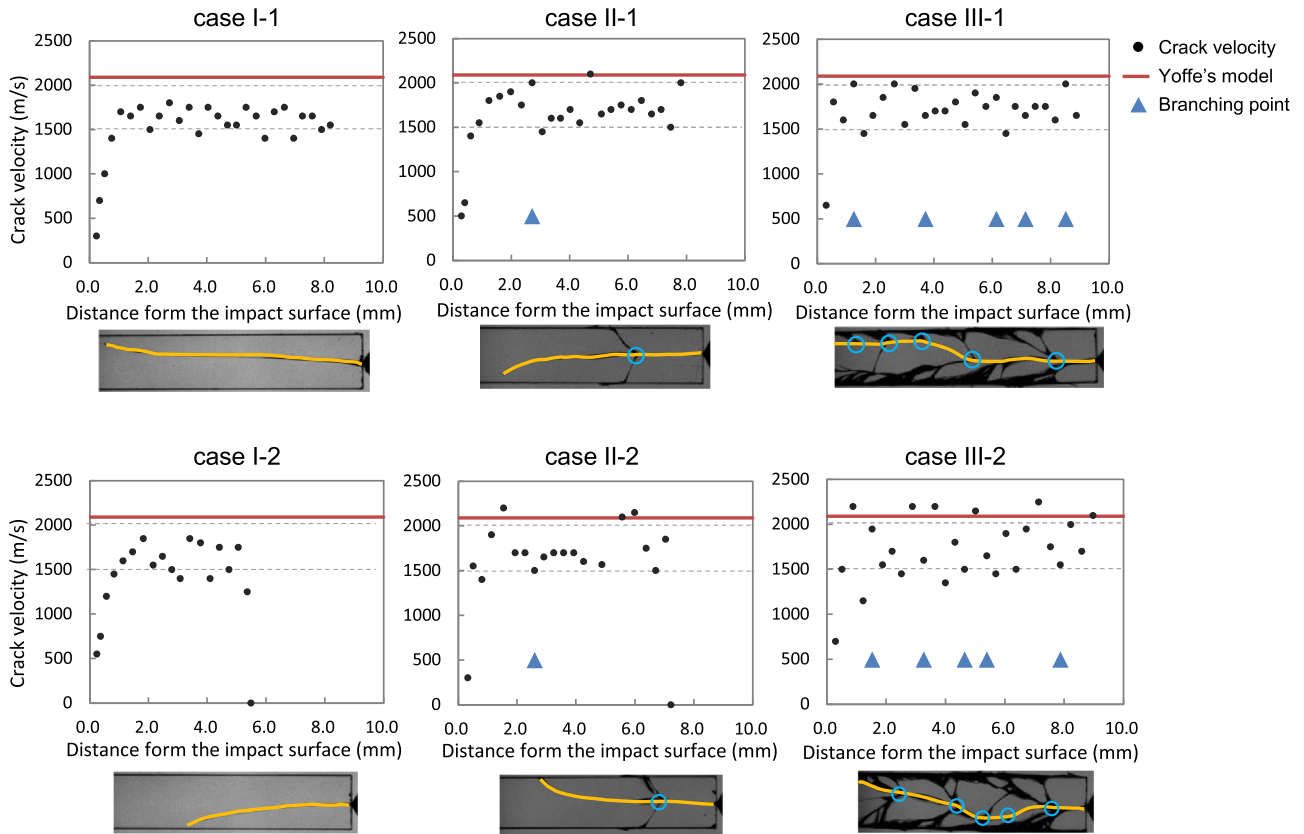
FIG. 7. Crack velocity versus the distance from the impact surface with the branching points in the experiments. The value of critical velocity $c_{cr} = 2090$ m/s given by Yoffe's model [43] is indicated by the red continuous lines in the graphs and the positions of the branching points are indicated by the blue triangles in the graphs. The crack velocity and the branching points were measured on the main crack in the field of view. The yellow (light gray) lines and the blue circles on the images of the crack patterns placed below each graph respectively show the main crack and the crack branching points used for the measurement.

velocity rapidly decreases near or below 2000 m/s. Therefore, it can be estimated that the critical velocity c_{cr} at which crack branches is about 2000 m/s for the chemically tempered glass sheets used in the experiments.

VI. NUMERICAL ANALYSIS OF DYNAMIC FRACTURE IN CHEMICALLY TEMPERED GLASS SHEETS

We performed the numerical analysis simulating the dynamic fracture experiments of chemically tempered glass sheets presented in the previous section.

A. Residual stress profile used in numerical analysis

We firstly determine the inelastic strain distributions which generates the residual stress profile of the three types of chemically tempered glass sheets used in experiments. We derived the distribution of K^+ in the glass sheet after immersing in KNO_3 salt bath from the following equation [44]:

$$c_z = c_0 + (c_{eq} - c_0) \left[\text{erfc} \frac{z}{2\sqrt{Dt}} - \exp\left(\frac{M}{D}z + \frac{M^2}{D}t\right) \right.$$
$$\left. \times \text{erfc}\left(\frac{z}{2\sqrt{Mt}} + \frac{M}{D}\sqrt{Dt}\right) \right], \tag{43}$$

where c_z is the concentration of K^+, $c_0 = 3.966$ mol% is the initial concentration of K^+, $c_{eq} = 13.57$ mol% is the equilibrium concentration of K^+ at the outer surface, $D = 6.71 \times 10^{-14}$ m^2/s is the diffusion coefficient, $M = 1.20 \times 10^{-8}$ m/s is the mass transfer coefficient, t is the ion exchange duration, and z is the distance from the outer surface in the thickness direction. The in-plane distribution of K^+ was uniform. Here we neglected the effect of the ion exchange on the side of the glass sheet. We prepared the finite-element model with the unstructured tetrahedral mesh of the uniform element size. The number of nodes was 48 580 232 and the number of elements was 304 643 588. The dimensions of the model were $l_x \times l_y \times l_z = 30 \times 2.0 \times 0.35$ mm, where l_z was the half of the thickness of the tempered glass sheet used in the experiments [see Fig. 8(a) for the axis direction]. Since the ion exchange process is performed at the temperature well below the glass annealing point, the distribution of the inelastic strain is given as $\epsilon_{ij}^p = A(c_z - c_0)\delta_{ij}$ in terms of c_z where $A = 0.001055$ is the linear network dilation coefficient and δ_{ij} is the Kronecker delta.

We statically solved the simultaneous equations (33) with the prescribed distribution of the inelastic strain ϵ_{ij}^p and the following prescribed displacement boundary conditions: u_z is constrained at $z = l_z$ plane, u_x is constrained on $y = 0$ at $z = l_z$ plane, and u_y is constrained on $x = 0$ at $z = l_z$
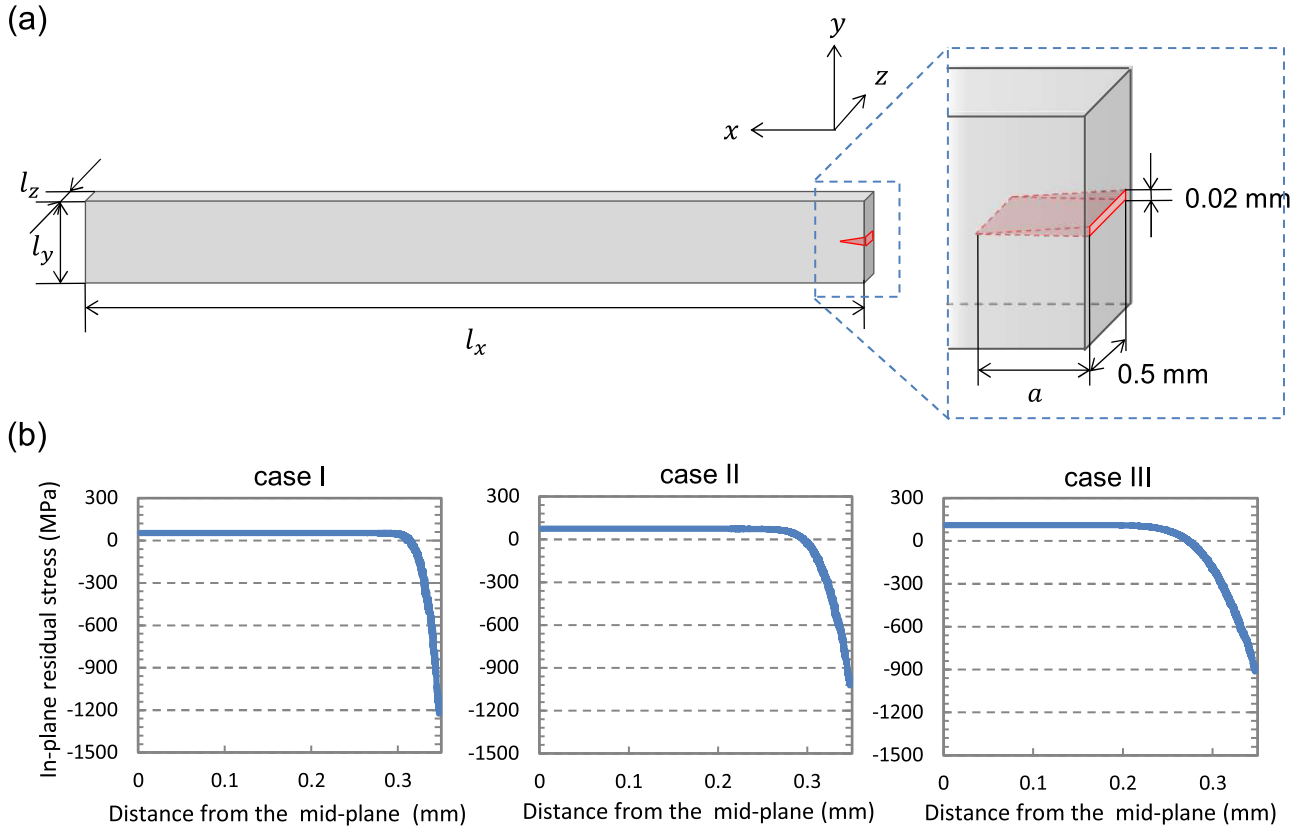
(a)

(b)

FIG. 8. Geometry of the analysis model and residual stress profiles of each analysis model. (a) The geometry of the analysis model with the initial crack. The initial crack is indicated by the red (dark gray) area. (b) The in-plane residual stress profiles (i.e., σ_{xx} or σ_{yy}) in the z direction for each analysis model. The horizontal axis expresses the distance from the midplane (i.e., $z = l_z/2$ plane) in the z direction. The in-plane residual stress profile is symmetrical with respect to the midplane in the z direction.

plane. Then, using the derived total displacement $u_i^{t\alpha}$, the residual stress of each element is given as $\sigma_{ij}^{\beta} = c_{ijkl}^{\beta}(\epsilon_{kl}^{t\beta} - \epsilon_{kl}^{p\beta})$; see Eqs. (30).

To adjust the residual stress profiles used in the numerical analyses to those of the chemically tempered glass sheets used in the experiments with respect to CT and DOL, we set the parameter t, D, and A for each case as shown in Table II. According to these parameter tunings, we obtained the residual stress profile for the numerical analyses; see the values of CT, CS, and DOL in Table II and the profile in Fig. 8. Since the crack propagation is mainly driven by the tensile residual stress, the mismatch of CS between the experiments and the numerical analyses does not have a significant influence on the crack pattern [8].

TABLE II. Parameters and CT, CS, and DOL for each analysis model.

	t (s)	D $\times 10^{-14}$ (m²/s)	A	CT (MPa)	CS (MPa)	DOL (µm)
case I	12 240	1.342	0.0015297	52.8	1220	40.0
case II	7 200	6.710	0.0014242	74.0	1020	55.0
case III	18 360	6.710	0.0012449	112	909.0	82.0

Then, we formed the finite-element model plane-symmetrically with respect to the $z = 0.35$ mm plane so that the thickness of the analysis model becomes the same as the chemically tempered glass sheets used in the experiments. Considering the symmetry, the distribution of $u_i^{t\alpha}$ and $\epsilon_{ij}^{p\beta}$ are assigned to the nodes or the elements of the symmetrically formed mesh. This mapping makes the self-equilibrated initial state of the dynamic fracture analysis with tetrahedral mesh satisfying Eq. (33).

B. Dynamic fracture analysis

We used the plane-symmetric finite-element model with the unstructured tetrahedral mesh of the uniform element size formed in the previous subsection for the fracture analysis. The dimensions of the model were $l_x \times l_y \times l_z = 30 \times 2.0 \times 0.70$ mm [see Fig. 8(a) for the axis direction]. The number of nodes was 96 049 195 and the number of elements was 609 287 176. The average nodal distance was 9.36 µm. Here the model dimension l_x was different from that of the samples used in the experiments to reduce the computational costs: 30 mm in the numerical analyses and 50 mm in the experiments. The difference of l_x affects the time-of-arrival of the elastic wave reflected by the boundary ($x = l_x$ plane) at the crack tip. However, the cracks pass through the visual field in the experiment (about 8–10 mm from the $x = 0$ plane)

TABLE III. Parameters for the dynamic fracture analysis.

Mass density	ρ	2500	kg/m^3
Young's modulus	E	74.0	GPa
Poisson's ratio	ν	0.22	
Surface energy	Γ	4.0625	J/m^2
Time increment	Δt	0.5	ns

faster than the arrival of the reflected elastic wave even if $l_x = 30$ mm, therefore the short l_x in the numerical analyses does not affect the crack patterns in the visual field.

At $t = 0.0$ s, the particle velocity of all the Voronoi particles are set to zero, and all the Voronoi boundaries in the area of initial crack are fractured; see the shape of the initial crack in Fig. 8(a). The equilibrium state of the internal force f_i^α is broken by this initial fracture and then the dynamic fracture process starts. Here the critical length of the initial crack a_{cr} to start the fracture in the numerical analysis depends on the intensity of the tensile residual stress. Within our parametric study for 0.2 mm $\leqslant a \leqslant 1.0$ mm, $a_{cr} = 0.4$ mm in the case I and $a_{cr} = 0.3$ mm in the case II and III. The crack did not propagate when $a < a_{cr}$. As long as $a_{cr} \leqslant a \leqslant 1.0$ mm, the general pattern of the cracks did not change even though the detailed crack paths were a little different. Therefore, we set the length of the initial crack as 0.5 mm for all cases in the numerical analyses so as to be sufficiently long against a_{cr}.

The time evolution of the dynamic behavior of the chemically tempered glass sheet given by Hamiltonian equations [Eqs. (39) and (40)] is solved by symplectic integrator (SI) [45] with the time increment Δt; see Appendix B. The time increment Δt for SI is set to become much less than the maximum limit of the time increment determined by Courant-Friedrichs-Lewy condition. The parameters used in the dynamic fracture analysis are shown in Table III. The traction-free boundary condition has been applied to all the nodes at the surface of the analysis model. At each time step,

all the Voronoi boundaries adjacent to the already fractured boundaries were examined whether they satisfy the fracture criterion. The fracture analysis is performed until the fracture process is completely terminated. The computing resource is a dual CPU processor sever with Intel Xeon Gold 6140. The typical computation time for 100 steps is about 1077 s and the computation time is linear to the number of nodes of the finite-element model.

C. Results of numerical analysis and discussion

The fracture patterns reproduced by the numerical analyses with the different residual stress profiles are presented in Fig. 9(a). These figures show the crack patterns projected on the xy plane. The fracture patterns obtained from the numerical analyses perfectly coincide with the experimental observations on every sample with different residual stress profiles; the crack does not bifurcate for case I, the crack branches only once to two or three cracks for case II, and the cracks repetitively branch and form complicated crack pattern for case III (the quantitative comparison of the fracture patterns for case III between the experiments and the numerical analysis is shown in Fig. 14).

Figure 9(b) shows the snapshot from the case I projected on the xz plane. The crack front proceeds in the tensile region and delays in the compressive region. This delay is due to the time lag between the crack penetration and the release of the compressive residual stress. The shape of the crack front in Fig. 9(b) coincides with that called "Wallner lines" generally observed in fracture of tempered glass sheets [46].

In addition to these features of crack patterns depending on the residual stress profile, the crack patterns of the numerical analyses projected on the xy plane also show the fanlike shape of the cracks near the edge of the glass sheet [Fig. 9(a)]. Figure 10 shows the crack surface in case I from a different angle and a magnified view of a part of the fanlike shape of the crack. According to this figure, the crack surface is folded
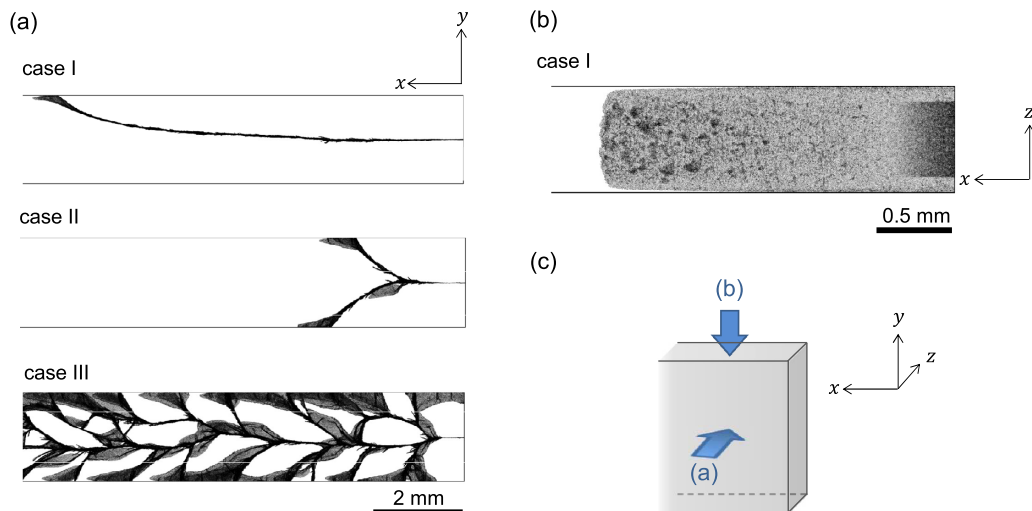

FIG. 9. Crack patterns of the chemically tempered glass sheets in the numerical analyses. (a) The crack patterns in the numerical analyses. These snapshots trim off the area of $x > 10$ mm. (b) The snapshot of the crack propagation in xz plane for case I at $t = 1.5$ μs. The crack does not fully propagate to the compressive layer near the crack tip. (c) The view angle for (a) and (b).
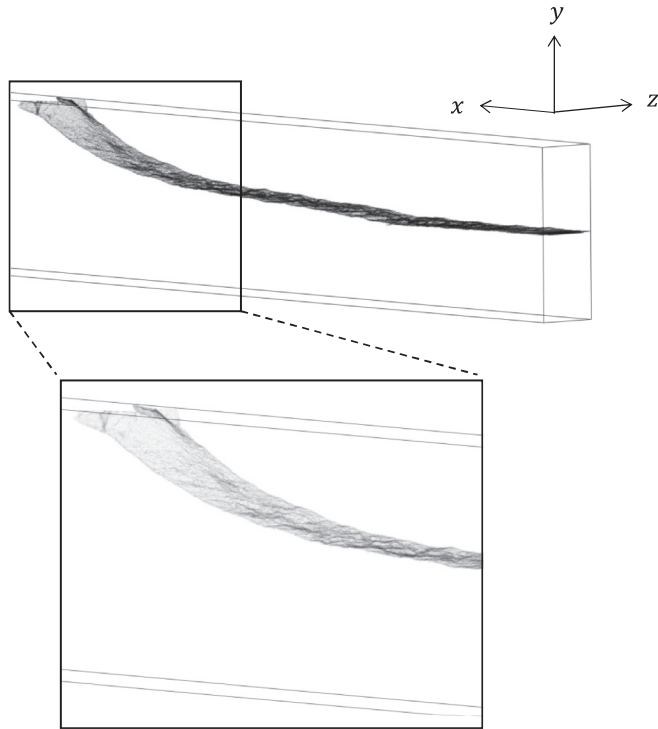
FIG. 10. Crack surface in case I from a different angle and a magnified view of a part of the fanlike shape of the crack.

when it approaches the edge of the glass sheet. This fold of the crack surface forms the fanlike shape of the cracks observed in experiments.

We measured the crack velocity of the models in numerical analyses (Fig. 11). The crack velocity was measured by using the JPEG snapshot images of the crack propagation process in the same manner as the experiments. Here, the time step Δt_v is 100 ns. As seen in the experiments (Fig. 7), the crack velocity transitions about between 1500 m/s and 2000 m/s. When the crack velocity almost reaches or exceeds 2000 m/s, the cracks branch and the crack velocity rapidly decreases

near or below 2000 m/s. The experiments and the numerical analyses show perfect agreement in all these characteristics of the crack velocity.

The estimated critical velocity $c_{cr} = 2000$ m/s in the experiments and the numerical analyses is about 57.4% of the shear wave speed c_s and 63.0% of the Rayleigh wave speed c_R, where $c_s = 3483$ m/s and $c_R = 3178$ m/s for the glass material used in the experiments. Theoretically, for a single crack propagating in solid continuum, Yoffe's model [43] predicts $c_{cr} \approx 0.6\,c_s$ and Eshelby [47] argues $c_{cr} \approx 0.5\,c_R$. Also, Sharon and Fineberg [48,49] shows $c_{cr} \approx 0.4\,c_R$ from the experiment using the normal float glass. These theories and experiments assume the crack propagating in a normal direction to the uniaxial tensile field. On the other hand, Tang *et al.* [50] analyze a Yoffe's crack moving at constant speed under the effect of T stress (i.e., the stress acting parallel to the crack). They state that the increase in T stress results in the decrease in c_{cr}/c_s. However, Raffie *et al.* [51], Zhan *et al.* [52], and the experiment by, e.g., Ravi-Chandar and Knauss [53] show that c_{cr} does not depend on the stress parallel to the crack. Thus, the explanation for the critical velocity for crack branching in complicated stress field is still a matter of debate.

The residual stress fields of the chemically tempered glass sheets are the equal biaxial tension and the inflow of the energy into the system due to external applied loadings does not exist. This field condition is completely different from the Yoffe's assumption [43]; however, within our study, the critical velocity of the experiments and the numerical analyses is most consistent with the Yoffe's model [43], $c_{cr} \approx 0.6\,c_s$.

Figure 12(a)–12(c) show the time history of the residual stress field at the midplane in the thickness direction; the midplane in the thickness direction has the maximum tensile residual stress. The maximum stress of the contour bands is changed in each analysis model. The elastic wave generated by the fracture propagates antecedent to the crack tips. Also, the stress concentrates at the crack tips and it is only released around the cracks. Contrary to stress field generated by applied external loadings, residual stress field is generated by the distributed internal force due to the spatial
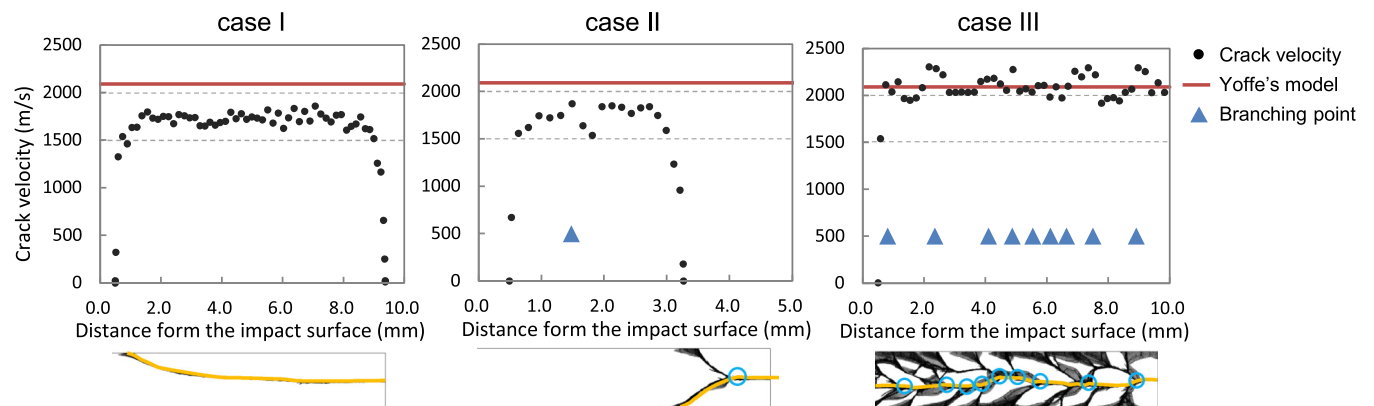

FIG. 11. Crack velocity versus the distance from the impact surface with the branching points in the numerical analyses. The value of critical velocity $c_{cr} = 2090$ m/s given by Yoffe's model [43] is indicated by the red continuous lines in the graphs and the positions of the branching points are indicated by the blue triangles in the graphs. The crack velocity and the branching points were measured on the main crack in the area of $x < 10$ mm. The yellow (light gray) lines and the blue circles on the images of the crack patterns placed below each graph respectively show the main crack and the crack branching points used for the measurement.
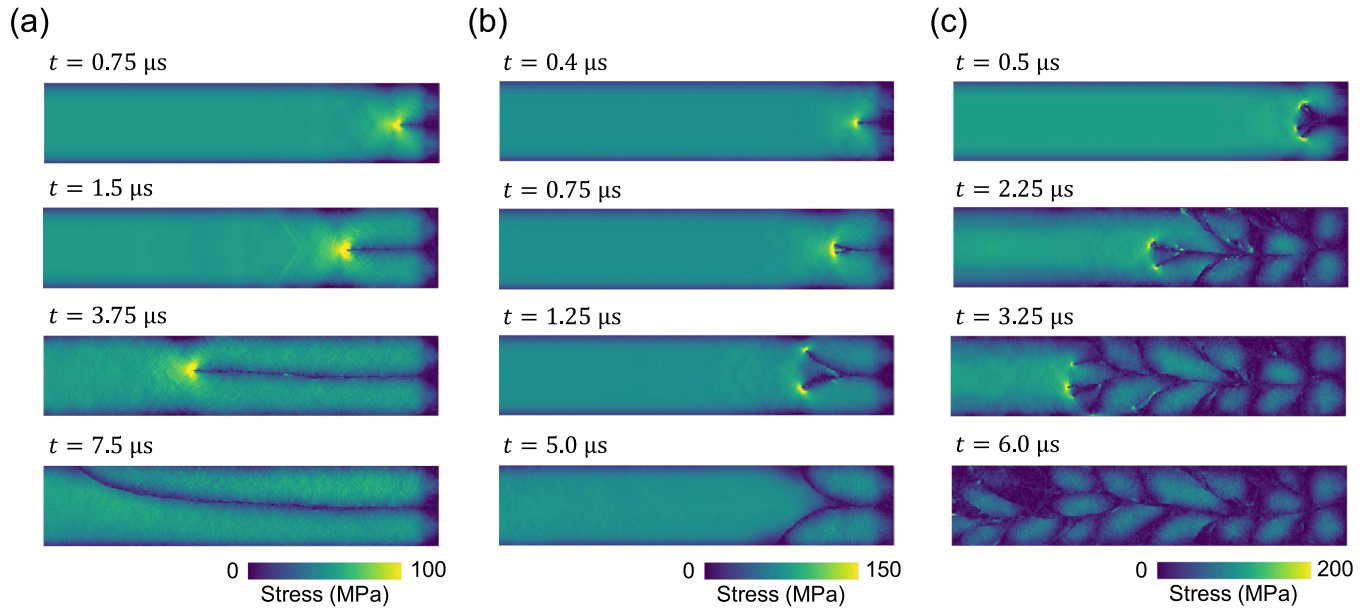
FIG. 12. Snapshots of the contours of the maximum principal stress at the midplane in the thickness direction. The elastic wave generated by the fracture can be observed antecedent to the crack tips in all cases. The stress concentrates at the crack tips. The concentric residual stress distributions are observed in each fragment. (a) Case I. (b) Case II. (c) Case III.

gradient of the inelastic strain [Eq. (34)]. Since this internal force keeps acting on every local area even after fracture, the residual stress remains in each isolated fragment. The remaining residual stress in the isolated fragments forms a concentric distribution: higher at the center of the fragment and lower at the periphery of the fragment. This remaining internal force causes repeated branching resulting in catastrophic failure as seen in case III.

The morphology of the shattered sheets of the tempered glass has been investigated to estimate the magnitude of the residual stress from the size of the fragments [7,8,54–56]. Also, Nielsen [23] presents the model for the estimation of the remaining strain energy in the fragments from the shape of the fragments and the initial residual stress field. However, these investigations are based on the simple models and the relationship between the size and/or shape of the fragments is still a matter of debate. Our approach rigorously evaluates the release and redistribution of the residual stress during fracture and therefore will make it possible to reveal the relationship between the shape of the fragments, the initial residual stress field, and the remaining strain energy in the fragments.

The videos for the crack propagation processes and the change in the maximum principal stress of the residual stress at the midplane in the thickness direction in the numerical analyses are shown in Supplemental Videos 4–6 [42] respectively corresponding to cases I, II, and III. The upper videos show the crack propagation and the lower videos show the contour of the maximum principal stress of the residual stress. These videos trim off the area of $x > 10$ mm. The real time durations for Supplemental Videos 4–6 are 7.5 μs, 5.0 μs, and 6.0 μs, respectively. The time magnifications of these videos are the same.

The agreement in the features of the crack patterns and the crack propagation process between the experiments

and the numerical analyses indicates that the release and the autonomous redistribution process of the residual stress field due to dynamic fracture are properly modeled and precisely evaluated by the numerical analysis method proposed in this paper. This is the most significant achievement of this research.

In addition to the results described above, we performed the study of convergence of the fracture patterns according to the element size of the tetrahedral mesh as shown in Fig. 13. Here, we studied on the unstructured mesh with different average nodal distance $d_{avg} = 18.7, 13.5, 9.36$ μm. For case I, the crack does not bifurcate on every mesh. For case II and III, the number of crack branching on the coarse mesh with $d_{avg} = 18.7$ μm is different from other two meshes. On the meshes with $d_{avg} = 13.5$ μm and $d_{avg} = 9.36$ μm, the number of crack branching and the basic features of the fracture patterns are almost coincident with each other (the quantitative comparison of fracture pattern for case III is shown in Fig. 14). Therefore, it is concluded that the fracture patterns do not converge on the mesh with $d_{avg} = 18.7$ μm and they converge when d_{avg} of a mesh is smaller than $d_{avg} = 13.5$ μm. In this paper, the comparison between the experiments and the numerical analysis is performed on the results using the mesh with $d_{avg} = 9.36$ μm; these results of the numerical analyses sufficiently converged.

We also measured the size of the fragments generated in case III for the quantitative comparison of the complicated fracture patterns. By using the figures of the fracture pattern projected on the xz plan, we measured area of the fragments (i.e., area of the white region in Fig. 6 and Fig. 13) completely included in the field of view. Figure 14 shows the scatter plot for the area of the fragments in case III. Here, we plotted the two results of the experiments and the three results of the numerical analyses with the different element size of the tetrahedral mesh shown in Fig. 13. In the experiments, the
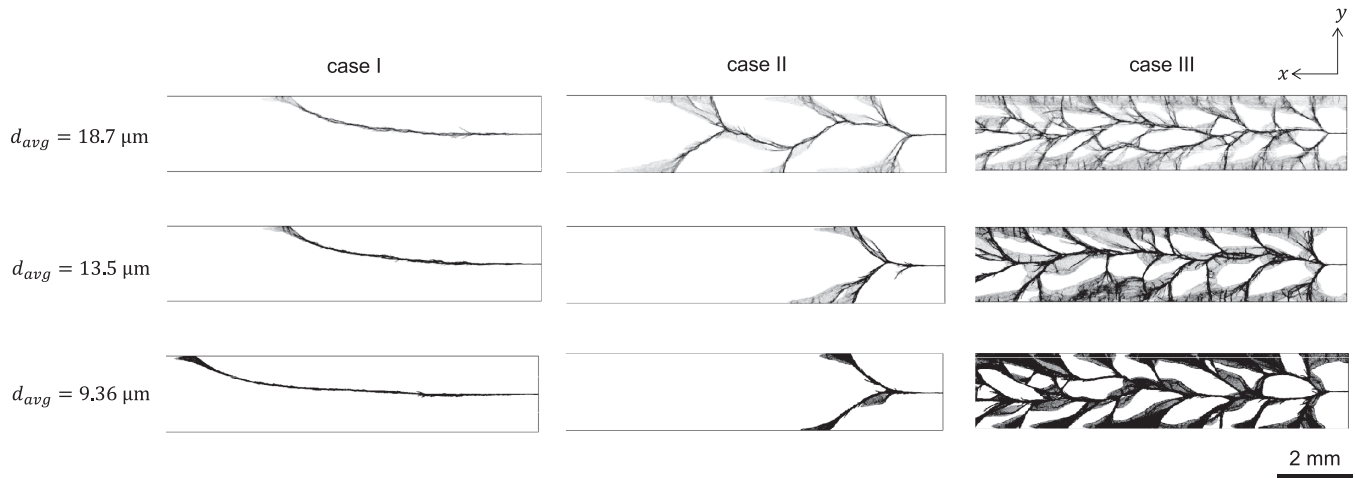
FIG. 13. Convergence of the fracture patterns according to the element size of the tetrahedral mesh. d_{avg} is the average nodal distance of the meshes.

distribution of area of the fragments is significantly different between the samples. This is because the cracks show dynamic instability under the high tensile residual stress. In the numerical analyses, the variation of area and the mean area converge when $d_{avg} \leqslant 13.5$ μm as described in the previous paragraph.
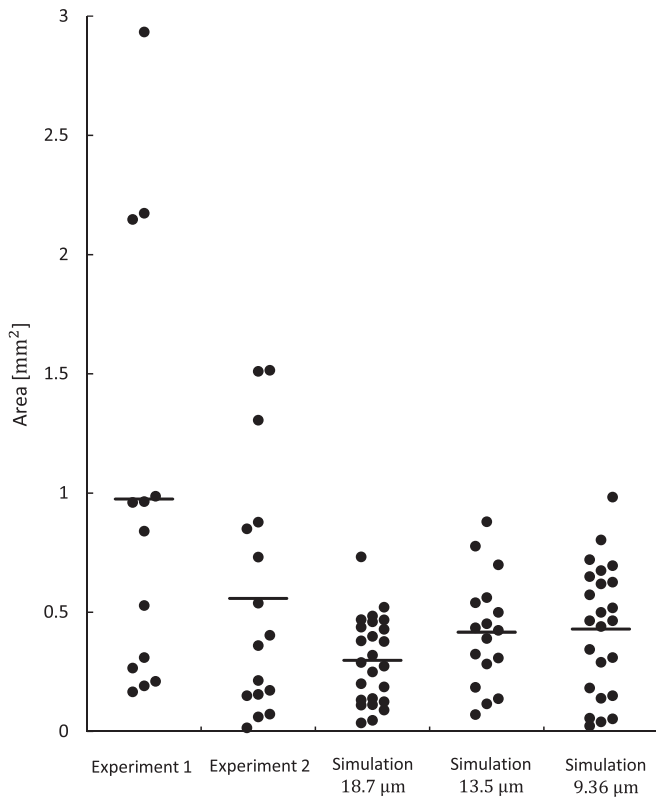

FIG. 14. Scatter plot for the area of the fragments generated by the fracture of case III in the experiments and the numerical analyses. The bars show the mean area of each result. Experiments 1 and 2 are corresponding to case III-1 and case III-2 in the experiments respectively and the lengths written in the horizontal axis label mean the average nodal distance d_{avg} of the tetrahedral mesh in the numerical analyses.

vious paragraph. Comparing among the experiments and the numerical analyses, the results of the numerical analyses show the smaller variation of area than the experimental results while the mean area of the numerical analyses is close to Experiment 2.

Before closing the discussion, relatively minor problems should be mentioned. In the numerical analyses, the surface energy Γ is 1.3 times larger than that of the chemically tempered glass sheets. In addition, though precise comparison may not be advisable because of the large variation of the experimental results of case III due to the crack instability, the number of cracks and the number of branching of the cracks appeared in the numerical analyses of case III [Fig. 9(a)] seem to be slightly larger than the experimental results of case III (Fig. 6). Also, the variation of area of the fragments in the numerical analyses of case III is smaller than that of the experimental results of case III; see Fig. 14. These mismatches could be mainly because of the energy dissipation modeling. In the numerical analysis, the energy dissipation results from the formation of the crack surfaces. Other sources of the energy dissipation such as attenuation, sound and/or heat have not been considered. Introduction of the effect of these energy dissipations in the model could reduce these discrepancies between numerical analysis results and experimental results. However, incorporating the dissipation model and modifying the parameters are required only when we have to customize the proposed numerical analysis method to the practical applications for the dynamic fracture of the tempered glass sheets. The agreements in the general features between the results from the numerical analyses and those from experiments shown in this paper can ensure the validity of the proposed method as a tool for the analysis of dynamic fracture in the residual stress field.

VII. CONCLUSION

This paper proposes the mathematical model and the numerical analysis method for the dynamic fracture in residual stress field. We formulate the Hamiltonian for the dynamic behavior of the solid continuum with residual stress field by

applying the particle discretization to the field variables in the context of PDS-FEM. Introducing the appropriate treatment of the fracture in residual stress field, this Hamiltonian formulation provides the rigorous evaluation of release and redistribution of the residual stress due to dynamic crack propagation. Our model suggests that the distributed internal force due to the inhomogeneous inelastic deformation plays a significant role in the dynamic fracture in residual stress field. This force keeps acting on every local area even in isolated fragments, and thereby causes the catastrophic fragmentation particularly observed in residual stress field.

To the best of the authors' knowledge, numerical simulation of dynamic fracture in residual stress field does not exist before our current attempt. According to our numerical analyses by using PDS-FEM, we suggest that (i) introduction of the self-equilibrated state to the continuum, (ii) the evaluation method for the residual stress in the partially fractured medium, and (iii) the dynamic fracture analysis with explicit time integration scheme are the most important points in the numerical analysis of the dynamic fracture in residual stress field. If these points can be properly addressed and implemented, it would be possible to simulate the dynamic fracture in residual stress field by using other numerical simulation methods.

The proposed numerical analysis method is validated by applying to the typical examples of the dynamic fracture in the residual stress field. The numerical analyses presented in this paper were performed on the dynamic fracture of chemically tempered glass sheets with different residual stress profiles. The results of the numerical analyses perfectly reproduce the crack patterns varying from single crack to catastrophic failure depending on the residual stress profile. Also, the experiments and the numerical analyses show remarkable agreement in the crack velocity and the critical velocity for the crack branching. These results imply that the proposed mathematical model and numerical analysis method capture the mechanism for dynamic fracture behavior of the solid continuum with residual stress field. Since our numerical analysis method properly models the release and the redistribution of the residual stress field due to dynamic fracture, it can rigorously evaluate the remaining residual stress in each fragment. This achievement will be able to settle the discussion for the relationship between the initial residual stress field and the size and/or shape of the fragments. We believe that this analysis method can be a prominent candidate for the prediction of the fracture processes in various materials with residual stress field.
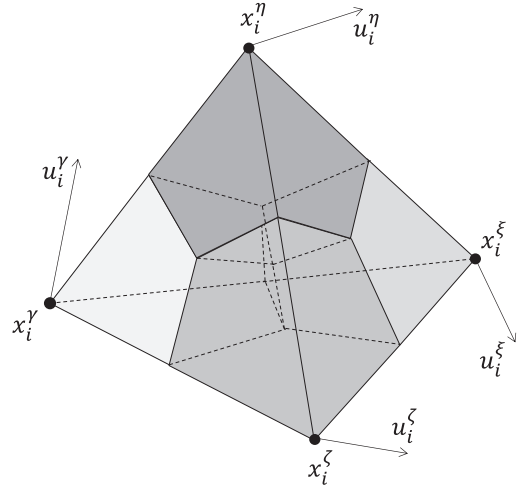
FIG. 15. The vertices and the nodal displacement vectors of the tetrahedral element Ψ^β.

APPENDIX A: EXPLICIT FORM OF $\epsilon_{ij}^{e\beta*}$ AND $\epsilon_{ij}^{p\beta*}$

When the distribution of the permanent inelastic strain $\epsilon_{ij}^{p\beta}$ is prescribed for all the element and no fracture exists in any element, the nodal displacement vector $u_i^{p\alpha}$ corresponding to $\epsilon_{ij}^{p\beta}$ can be formally expressed as

$$\epsilon_{ij}^{p\beta} = \sum_{\alpha=1}^{N} \frac{1}{2} \left(B_j^{\beta\alpha} u_i^{p\alpha} + B_i^{\beta\alpha} u_j^{p\alpha} \right). \tag{A1}$$

Likewise, when the βth element has fracture surfaces in it,

$$\epsilon_{ij}^{p\beta*} = \sum_{\alpha=1}^{N} \frac{1}{2} \left(B_j^{\beta\alpha*} u_i^{p\alpha} + B_i^{\beta\alpha*} u_j^{p\alpha} \right). \tag{A2}$$

Note that the nodal displacement vector $u_i^{p\alpha}$ does not change before and after the fracture. For the rigorous evaluation of $\epsilon_{ij}^{p\beta*}$ (the permanent inelastic strain in the elements with fracture surfaces), $u_i^{p\alpha}$ corresponding to $\epsilon_{ij}^{p\beta}$ (the prescribed inelastic strain in the elements without fracture surface) should be identified. However, the element-wise equations (A1) for each component of the prescribed $\epsilon_{ij}^{p\beta}$ are a degenerate set of the equations, and thus, $u_i^{p\alpha}$ is left with the ambiguity in the rigid body translation and the rigid body rotation of the element. To overcome this problem, we consider the element-wise $u_i^{p\alpha}$ without rigid body displacement in each element. Since the rigid body displacement of an element does not contribute to the strain in an element, the element-wise nodal displacement vector $u_i^{p\alpha}$ without rigid body displacement in each element can be safely used as the permanent displacement vector corresponding to the prescribed $\epsilon_{ij}^{p\beta}$.

Let $x_i^\eta, x_i^\gamma, x_i^\zeta$, and x_i^ξ be the position vectors of the vertices of the βth tetrahedral element (i.e., the mother points of the Voronoi particles composing the βth element) and let u_i^η, u_i^γ, u_i^ζ, u_i^ξ be the displacement vectors of the Voronoi particles composing Ψ^β, see Fig. 15. The constraint condition corresponding to zero rigid body translation is

$$u_i^\eta = 0 \tag{A3}$$

and the constraint conditions corresponding to zero rigid body rotation are

$$u_i^\gamma = a\left(x_i^\gamma - x_i^\eta\right), \tag{A4}$$

$$u_i^\zeta = b\left(x_i^\gamma - x_i^\eta\right) + c\left(x_i^\zeta - x_i^\eta\right), \tag{A5}$$

surfaces, the components of $\epsilon_{ij}^{p\beta}$ can be written as

$$\epsilon_{11}^{p\beta} = aB_1^{\beta\gamma}\left(x_1^\gamma - x_1^\eta\right) + bB_1^{\beta\zeta}\left(x_1^\gamma - x_1^\eta\right) + cB_1^{\beta\zeta}\left(x_1^\zeta - x_1^\eta\right) + B_1^{\beta\xi}u_1^\xi$$

$$\epsilon_{22}^{p\beta} = aB_2^{\beta\gamma}\left(x_2^\gamma - x_2^\eta\right) + bB_2^{\beta\zeta}\left(x_2^\gamma - x_2^\eta\right) + cB_2^{\beta\zeta}\left(x_2^\zeta - x_2^\eta\right) + B_2^{\beta\xi}u_2^\xi$$

$$\epsilon_{33}^{p\beta} = aB_3^{\beta\gamma}\left(x_3^\gamma - x_3^\eta\right) + bB_3^{\beta\zeta}\left(x_3^\gamma - x_3^\eta\right) + cB_3^{\beta\zeta}\left(x_3^\zeta - x_3^\eta\right) + B_3^{\beta\xi}u_3^\xi$$

$$2\epsilon_{12}^{p\beta} = a\left\{B_2^{\beta\gamma}\left(x_1^\gamma - x_1^\eta\right) + B_1^{\beta\gamma}\left(x_2^\gamma - x_2^\eta\right)\right\} + b\left\{B_2^{\beta\zeta}\left(x_1^\gamma - x_1^\eta\right) + B_1^{\beta\zeta}\left(x_2^\gamma - x_2^\eta\right)\right\}$$

$$+ c\left\{B_2^{\beta\zeta}\left(x_1^\zeta - x_1^\eta\right) + B_1^{\beta\zeta}\left(x_2^\zeta - x_2^\eta\right)\right\} + B_2^{\beta\xi}u_1^\xi + B_1^{\beta\xi}u_2^\xi$$

$$2\epsilon_{23}^{p\beta} = a\left\{B_3^{\beta\gamma}\left(x_2^\gamma - x_2^\eta\right) + B_2^{\beta\gamma}\left(x_3^\gamma - x_3^\eta\right)\right\} + b\left\{B_3^{\beta\zeta}\left(x_2^\gamma - x_2^\eta\right) + B_2^{\beta\zeta}\left(x_3^\gamma - x_3^\eta\right)\right\}$$

$$+ c\left\{B_3^{\beta\zeta}\left(x_2^\zeta - x_2^\eta\right) + B_2^{\beta\zeta}\left(x_3^\zeta - x_3^\eta\right)\right\} + B_3^{\beta\xi}u_2^\xi + B_2^{\beta\xi}u_3^\xi$$

$$2\epsilon_{31}^{p\beta} = a\left\{B_3^{\beta\gamma}\left(x_1^\gamma - x_1^\eta\right) + B_1^{\beta\gamma}\left(x_3^\gamma - x_3^\eta\right)\right\} + b\left\{B_3^{\beta\zeta}\left(x_1^\gamma - x_1^\eta\right) + B_1^{\beta\zeta}\left(x_3^\gamma - x_3^\eta\right)\right\}$$

$$+ c\left\{B_3^{\beta\zeta}\left(x_1^\zeta - x_1^\eta\right) + B_1^{\beta\zeta}\left(x_3^\zeta - x_3^\eta\right)\right\} + B_3^{\beta\xi}u_1^\xi + B_1^{\beta\xi}u_3^\xi. \tag{A6}$$

Equation (A6) can be rearranged in the matrix form as

$$\boldsymbol{\epsilon}^{p\beta} = A\boldsymbol{u}^{p\beta}, \tag{A7}$$

where $\boldsymbol{\epsilon}^{p\beta} = [\epsilon_{11}^{p\beta}, \epsilon_{22}^{p\beta}, \epsilon_{33}^{p\beta}, \epsilon_{12}^{p\beta}, \epsilon_{23}^{p\beta}, \epsilon_{31}^{p\beta}]^T$ and $\boldsymbol{u}^{p\beta} = [a, b, c, u_1^\xi, u_2^\xi, u_3^\xi]^T$. The matrix A consists of $B_i^{\beta\gamma}$, $B_i^{\beta\zeta}$, $B_i^{\beta\xi}$, x_i^η, x_i^γ, and x_i^ζ. Since the inverse matrix of A always exists for the nondegenerate tetrahedrons, six unknown quantities related to $u_i^{p\alpha}$ (i.e., a, b, c, u_1^ξ, u_2^ξ, and u_3^ξ) can be determined. Therefore, using the constraint conditions (A3)–(A5), the element-wise nodal displacement vector $u_i^{p\alpha}$ without rigid body displacement for Ψ^β (i.e., u_i^η, u_i^γ, u_i^ζ, and u_i^ξ) can be determined. Substitution of this $u_i^{p\alpha}$ to Eq. (A2) gives the explicit form of the $\epsilon_{ij}^{p\beta*}$.

From Eq. (28), the elastic strain $\epsilon_{ij}^{e\beta*}$ in Eq. (41) is given as

$$\epsilon_{ij}^{e\beta*} = \epsilon_{ij}^{t\beta*} - \epsilon_{ij}^{p\beta*}, \tag{A8}$$

where

$$\epsilon_{ij}^{t\beta*} = \sum_{\alpha=1}^N \frac{1}{2}\left(B_j^{\beta\alpha*}u_i^{t\alpha} + B_i^{\beta\alpha*}u_j^{t\alpha}\right). \tag{A9}$$

Therefore, the elastic strain $\epsilon_{ij}^{e\beta*}$ in the fractured element Ψ^β can be written in terms of the displacement-strain matrix as

$$\epsilon_{ij}^{e\beta*} = \sum_{\alpha=1}^N \frac{1}{2}\left\{B_j^{\beta\alpha*}\left(u_i^{t\alpha} - u_i^{p\alpha}\right) + B_i^{\beta\alpha*}\left(u_j^{t\alpha} - u_j^{p\alpha}\right)\right\}. \tag{A10}$$

When the distribution of the permanent inelastic strain $\epsilon_{ij}^{p\beta}$ is prescribed, the displacement $u_i^{t\alpha}$ can be obtained through the symplectic integration of the Hamiltonian equations in each time step; see Sec. IV. Since we already have the explicit form of $u_i^{p\alpha}$, the explicit form of the elastic

where, a, b, and c are the constant scalar quantities.

Introducing the constraint conditions Eqs. (A3)–(A5) to the displacement-strain relationship (A1) for Ψ^β without fracture

strain $\epsilon_{ij}^{e\beta*}$ in the fractured element Ψ^β also can be obtained through Eq. (A10).

APPENDIX B: SYMPLECTIC INTEGRATOR

For the accurate numerical integration of Hamiltonian equations [Eq. (26) and Eq. (27)], we employ the SI [45]. The SI is an energy conserving numerical integration scheme for Hamiltonian systems. Here we show the algorithm for the nth-order bilateral SI. $u_i^\alpha(t)$ is the displacement of the αth Voronoi particle at time t and $p_i^\alpha(t)$ is the momentum of the αth Voronoi particle at time t. When $u_i^\alpha(t)$ and $p_i^\alpha(t)$ are expressed as $(u_i^{\alpha(0)}, p_i^{\alpha(0)})$,

$$\left(u_i^{\alpha(0)}, p_i^{\alpha(0)}\right) = \left(u_i^\alpha(t), p_i^\alpha(t)\right), \tag{B1}$$

$$u_i^{\alpha(k)} = u_i^{\alpha(k-1)} + \Delta t\, c^{(k)} \frac{\partial H}{\partial p_i^\alpha}\bigg|_{p_i^{\alpha(k-1)}}, \tag{B2}$$

$$p_i^{\alpha(k)} = p_i^{\alpha(k-1)} - \Delta t\, d^{(k)} \frac{\partial H}{\partial u_i^\alpha}\bigg|_{u_i^{\alpha(k)}} \tag{B3}$$

for $k = 1 \cdots n$,

$$p_i^{\alpha(h)} = p_i^{\alpha(h-1)} - \Delta t\, c^{(h-n)} \frac{\partial H}{\partial u_i^\alpha}\bigg|_{u_i^{\alpha(h-1)}}, \tag{B4}$$

$$u_i^{\alpha(h)} = u_i^{\alpha(h-1)} + \Delta t\, d^{(h-n)} \frac{\partial H}{\partial p_i^\alpha}\bigg|_{p_i^{\alpha(h)}} \tag{B5}$$

for $h = n + 1 \cdots 2n$,

$$\left(u_i^\alpha(t + 2\Delta t), p_i^\alpha(t + 2\Delta t)\right) = \left(u_i^{\alpha(2n)}, p_i^{\alpha(2n)}\right), \tag{B6}$$

where $c^{(k)}$ and $d^{(k)}$ are the symplectic coefficients, and Δt is the time increment.

The numerical analyses presented in this paper use the fourth-order bilateral symplectic algorithm. In this case, the

symplectic coefficients are

$$c^{(1)} = 0$$

$$c^{(2)} = c^{(4)} = 1/(2 - 2^{1/3})$$

$$c^{(3)} = 1/(1 - 2^{2/3})$$

$$d^{(1)} = d^{(4)} = (2 + 2^{1/3} + 2^{-1/3})/6$$

$$d^{(2)} = d^{(3)} = (1 - 2^{1/3} - 2^{1/3})/6 \,. \tag{B7}$$

[1] J. Le, L. Song, X. Peng, and X. Hu, Fracture mechanics analysis of thermally tempered glass plate: Fracture induced by an embedded crack, Int. J. Fract. **132**, 299 (2005).

[2] A. Koike, M. Tomozawa, and S. Ito, Sub-critical crack growth rate of soda-lime-silicate glass and less brittle glass as a function of fictive temperature, J. Non. Cryst. Solids. **353**, 2675 (2007).

[3] S. Karlsson, B. Jonson, and C. Stålhandske, The technology of chemical glass strengthening-A review, Glass Technol.: Eur. J. Glass Sci. Technol. A **51**, 41 (2010).

[4] A. K. Varshneya, Chemical strengthening of glass: Lessons learned and yet to be learned, Int. J. Appl. Glass. Sci. **1**, 131 (2010).

[5] G. Macrelli, Chemically strengthened glass by ion exchange: Strength evaluation, Int. J. Appl. Glass. Sci. **9**, 156 (2017).

[6] E. H. Lee, T. G. Rogers, and T. C. Woo, Residual stresses in a glass plate cooled symmetrically from both surfaces, J. Am. Ceram. Soc. **48**, 480 (1965).

[7] K. Akeyoshi, *Study on the Physical Tempering of Glass Plates-1-Effects of Thermal Conditions on Permanent Stress and Fragment Density of Tempered Glass Plates*, Tech. Rep. 1 (Reports of the Research Laboratory, Asahi Glass, 1967).

[8] J. M. Barsom, Fracture of tempered glass, J. Am. Ceram. Soc. **51**, 75 (1968).

[9] T. Sakai, M. Ramulu, A. Ghosh, and R. C. Bradt, Cascadating fracture in a laminated tempered safety glass panel, Int. J. Fract. **48**, 49 (1991).

[10] M. Overend, S. De Gaetano, and M. Haldimann, Diagnostic interpretation of glass failure, Syruct. Eng. Int. **17**, 151 (2007).

[11] J. H. Nielsen, J. F. Olesen, and H. Stang, The fracture process of tempered soda-lime-silica glass, Exp Mech. **49**, 855 (2009).

[12] M. M. Chaudhri and C. Liangyi, The catastrophic failure of thermally tempered glass caused by small-particle impact, Nature **320**, 48 (1986).

[13] K. Takahashi, S. I. Aratani, and Y. Yamauchi, Dynamic fracture in zone-tempered glasses observed by high-speed photoelastic colour photography, J. Mater. Sci. Lett. **11**, 15 (1992).

[14] K. Takahashi, Fast fracture in tempered glass, Key Eng. Mater. **166**, 9 (1999).

[15] S. Aratani, Estimation of the stress σ_{CR} generated at propagating crack front, J. Ceram. Soc. Jpn. **126**, 246 (2018).

[16] R. Harilal, C. P. Vyasarayani, and M. Ramji, A linear least squares approach for evaluation of crack tip stress field parameters using DIC, Opt. Lasers Eng. **75**, 95 (2015).

[17] H. B. Zeng and P. Bailly, Experimental characterization of dynamic behavior of gelatin-based material using DIC, Polym. Test. **63**, 298 (2017).

[18] M. Rossi, L. Cortese, K. Genovese, A. Lattanzi, F. Nalli, and F. Pierron, Evaluation of volume deformation from surface DIC measurement, Exp. Mech. **58**, 1181 (2018).

[19] M. L. L. Wijerathne, K. Oguni, and M. Hori, Tensor field tomography based on 3D photoelasticity, Mech. Mater. **34**, 533 (2002).

[20] M. L. L. Wijerathne, K. Oguni, and M. Hori, Stress field tomography based on 3D photoelasticity, J. Mech. Phys. Solids **56**, 1065 (2008).

[21] H. Aben, J. Anton, M. Paemurru, and M. Õis, A new method for tempering stress mesurement in glass panels, Est. J. Eng. **19**, 292 (2013).

[22] R. Dugnani, R. J. Zednik, and P. Verghese, Analytical model of dynamic crack evolution in tempered and strengthened glass plates, Int. J. Fract. **190**, 75 (2014).

[23] J. H. Nielsen, Remaining stress-state ans strain-energy in tempered glass fragments, Glass Struct. Eng. **2**, 45 (2017).

[24] J. H. Nielsen and M. Bjarrum, Deformations and strain energy in fragments of tempered glass: Experimental and numerical investigation, Glass Struct. Eng. **2**, 133 (2017).

[25] T. Belytschko and T. Black, Elastic crack growth in finite elements with minimal remeshing, Int. J. Numer. Meth. Eng. **45**, 601 (1999).

[26] N. Moës, J. Dolbow and T. Belytschko, A finite element method for crack growth without remeshing, Int. J. Numer. Meth. Eng. **46**, 131 (1999).

[27] T. Belytschko, N. Moës, S. Usui, and C. Parimi, Arbitrary discontinuities in finite elements, Int. J. Numer. Meth. Eng. **50**, 993 (2001).

[28] C. Shet and N. Chandra, Analysis of energy balance when using cohesive zone models to simulate fracture processes, J. Eng. Mater-T ASME **124**, 440 (2002).

[29] K. Y. Volokh, Comparison between cohesive zone models, Comm. Numer. Meth. Eng **20**, 845 (2004).

[30] G. A. Francfort and J. J. Marigo, Revisiting brittle fracture as an energy minimization problem, J. Mech. Phys. Solids **46**, 1319 (1998).

[31] B. Bourdin, A. F. Gilles, and J. J. Marigo, Numerical experiments in revisited brittle fracture, J. Mech. Phys. Solids **48**, 797 (2000).

[32] S. A. Silling, Reformulation of elasticity theory for discontinuities and long-range forces, J. Mech. Phys. Solids **48**, 175 (2000).

[33] S. A. Silling, M. Epton, O. Weckner, J. Xu, and E. Askari, Peridynamic states and constitutive modeling, J. Elast. **88**, 151 (2007).

[34] M. Hori, K. Oguni, and H. Sakaguchi, Proposal of FEM implemented with particle discretization for analysis of failure phenomenon, J. Mech. Phys. Solids **53**, 681 (2005).

[35] N. Kame, S. Saito, and K. Oguni, Quasi-static analysis of strike fault growth in layered media, Geophys. J. Int. **173**, 309 (2008).

[36] K. Oguni, M. L. L. Wijerathne, T. Okinaka, and M. Hori, Crack propagation analysis using PDS-FEM and comparison with fracture experiment, Mech. Mater. **41**, 1242 (2009).

[37] M. L. L. Wijerathne, K. Oguni, and M. Hori, Numerical analysis of growing crack problems using particle discretization scheme, Int. J Numer. Meth. Eng. **80**, 46 (2009).

[38] S. Hirobe, K. Imakita, H. Aizawa, Y. Kato, S. Urata, and K. Oguni, Simulation of Catastrophic Failure in a Residual Stress Field, Phys. Rev. Lett. **127**, 064301 (2021).

[39] S. Hirobe and K. Oguni, Coupling analysis of pattern formation in desiccation cracks, Comput. Methods Appl. Mech. Eng. **307**, 470 (2016).

[40] S. Hirobe and K. Oguni, Modeling and numerical investigations for hierarchical pattern formation in desiccation cracking, Physica D **359**, 29 (2017).

[41] A. A. Griffith, The phenomena of rupture and flow in solids, Philos. Trans. R. Soc. Lond. **221**, 163 (1921).

[42] See Supplemental Material at http://link.aps.org/supplemental/10.1103/PhysRevE.104.025001 for videos.

[43] E. H. Yoffe, The moving griffith crack, Phil. Mag. **42**, 739 (1951).

[44] M. Hatano, S. Kanasugi, and M. Konoshi, Temperature dependencies of inter-diffusion coefficient and mass-transfer coefficient of chemical strengthening, Key. Eng. Mater. **702**, 32 (2016).

[45] L. Casetti, Efficient symplectic algorithms for numerical simulations of hamiltonian flows, Phys. Scr. **51**, 29 (1995).

[46] R. Gardon, in *Glass: Science and Technology, Elasticity and Strength in Glasses*, edited by D. R. Uhlmann and N. J. Kreidl (Academic Press, New York, 1980), Vol. 5.

[47] J. D. Eshelby, Fracture mechanics, Sci. Prog. **59**, 161 (1971).

[48] E. Sharon and J. Fineberg, Microbranching instability and the dynamic fracture of brittle materials, Phys. Rev. B **54**, 7128 (1996).

[49] E. Sharon and J. Fineberg, Confirming the continuum theory of dynamic brittle fracture for fast cracks, Nature **397**, 333 (1999).

[50] B. Q. Tang, G. J. Tang, and X. F. Li, Effect of T-stress on branch angle of moving cracks, Mech. Res. Commun. **56**, 26 (2014).

[51] S. Raffie, T. H. Seelig, and D. Gross, Simulation of dynamic crack curving and branching under biaxial loading by a time domain boundary integral equation method, Int. J. Fract. **120**, 545 (2003).

[52] Y. B. Zhan, C. A. Tang, H. Li, Z. Z. Liang, S. B. Tang, and Y. F. Yang, Numerical investigation of dynamic crack branching under biaxial loading, Int. J. Fract. **176**, 151 (2012).

[53] K. Ravi-Chandar and W. G. Knauss, An experimental investigation into dynamic fracture: Iii. On steady-state crack propagation and crack branching, Int. J. Fract. **26**, 141 (1984).

[54] D. R. Oakley, Crack branching in float glass subjected to biaxial loading, J. Non. Cryst. Solids. **196**, 139 (1996).

[55] A. I. Shutov, P. B. Popov, and A. B. Bubeev, Prediction of the character of tempered glass fracture, Glass Ceram. **55**, 8 (1998).

[56] H. Lee, S. Cho, K. Yoon, and J. Lee, Glass thickness and fragmentation behavior in stressed glasses, N. J. Glass Ceram. **2**, 116 (2012).